




Research Paper

High-heat transfer lithium-ion batteries: A new era in battery thermal management

Alfred J. Piggott^{a,*}, Jeffrey S. Allen^b, Ahmad A. Pesaran^c 

^a Applied Thermoelectric Solutions LLC, 28175 Haggerty Road., Novi, MI 48377, USA

^b Mechanical and Aerospace Engineering, Michigan Technological University, 1400 Townsend Drive, Houghton, MI 49931, USA

^c National Renewable Energy Laboratory, 15013 Denver West Park way, Golden, CO 80401, USA

ARTICLE INFO

Keywords:

High heat transfer (HHT) batteries
Battery thermal management (BTM)
ParaThermic® battery
ThermalConnect®
Extreme fast charging (XFC)
Battery safety
Battery cooling

ABSTRACT

Despite advances in lithium-ion battery technology, critical challenges remain that must be addressed to accelerate electric vehicle (EV) adoption and global energy transformation. Significantly improved battery thermal management (BTM) is key to overcoming these challenges. BTM approaches focus on increasing heat transfer coefficients via air, liquid, or refrigerant cooling, but less attention is given to reducing the battery's thermal resistance, a major bottleneck for heat transfer. This work introduces a novel approach to reduce battery thermal resistance by integrating in-plane heat transfer with optimized cell geometry, minimized thermal resistances, and reduced interfacial resistances, representing a departure from previous methods. The standard prismatic can cell incorporating this technology is referred to as the high heat transfer (HHT) battery. An equivalent resistance battery thermal model is developed for speed and accuracy, validated against experimental data in the literature, demonstrating strong correlation and ensuring reliable predictions for real-world performance. Thermal performance metrics of the conventional and HHT batteries are compared using a parametric study with air, liquid, and refrigerant boundary conditions across a range of aspect ratios. The HHT battery shows a heat removal rate up to 20 times higher than a conventional battery. These findings suggest that HHT technology could be transformative for EV battery performance, enabling fast charging, mitigating thermal runaway, extending battery life, reducing cold-weather power loss, increasing reliability, lowering costs, and enabling higher energy density, all critical for EV adoption and energy transformation. Future work will focus on prototyping and real-world testing to refine these findings for commercial-scale applications.

1. Introduction

The United States is actively working to decarbonize the transportation sector by expanding the market share of zero-emission electric vehicles (EVs) [1]. To accelerate this transition, energy regulatory agencies and EV manufacturers have identified several critical areas for improvement in EV battery technology. These include battery energy density, capacity, life, reliability, safety, decreased battery costs, increased battery charge rate, and improved range retention of the battery in cold weather [2]. Temperature plays a significant role in influencing all of these factors, making advanced battery thermal management (BTM) a crucial solution for optimizing battery performance [3–7].

Heat is generated within a battery during the processes of charging and discharging due to the ohmic resistance of the cells and various entropic reactions. If this heat is not dissipated at a rate that matches its

generation, the battery's temperature will rise. If the temperature is allowed to fall below or exceed certain limits, the result could be battery degradation, performance loss and potential safety hazards [8–10].

The process of removing heat from an automotive battery during cooling can be categorized into three main stages illustrated in Fig. 1. The initial stage involves heat movement from the internal volume of the battery to its surface shown in Fig. 1a. The subsequent stage is managed by the battery thermal management system, which facilitates the movement of heat from the battery surface to either directly to the surrounding air or to a radiator. This second stage shown in Fig. 1b is typically accomplished with a cooling system that utilizes air, liquid or refrigerant as the cooling medium. Finally, if a radiator is employed, the last stage entails transferring heat from the radiator (illustrated in Fig. 1c) to the ambient air. The primary emphasis of this work is on the initial stage, which involves the transfer of heat from the volume of the battery cell to its exterior surface.

* Corresponding author.

E-mail addresses: Alfred@ThermoelectricSolutions.com (A.J. Piggott), jeffrey.allen@mtu.edu (J.S. Allen), ahmad.pesaran@nrel.gov (A.A. Pesaran).

<https://doi.org/10.1016/j.applthermaleng.2025.126347>

Received 17 December 2024; Received in revised form 17 February 2025; Accepted 26 March 2025

Available online 4 April 2025

1359-4311/© 2025 The Authors. Published by Elsevier Ltd. This is an open access article under the CC BY license (<http://creativecommons.org/licenses/by/4.0/>).

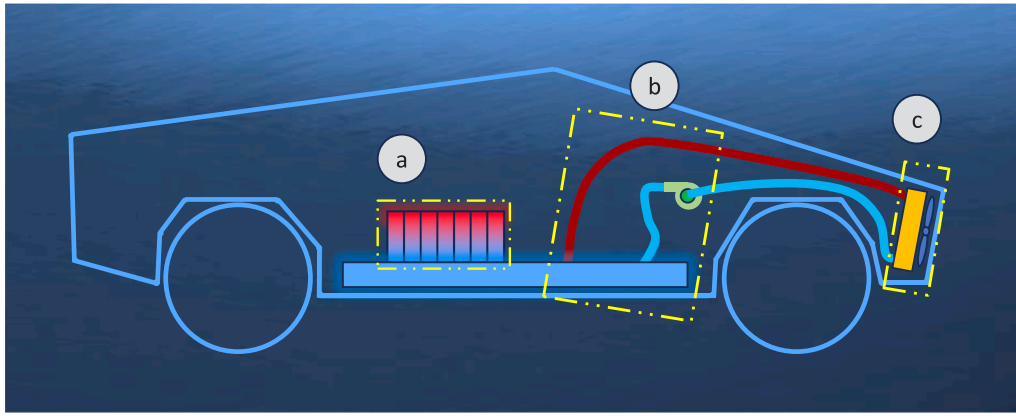


Fig. 1. Vehicle battery cooling system example (a) batteries (b) cooling system (c) radiator.

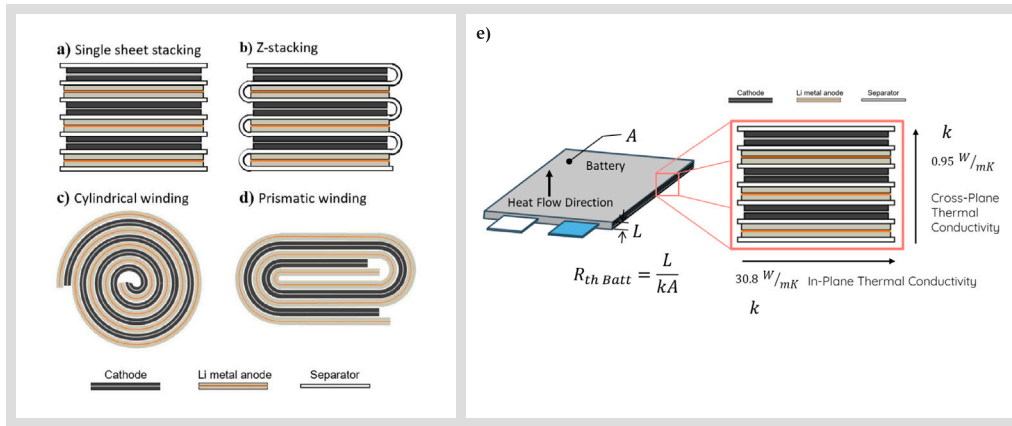


Fig. 2. Schematic of three battery cell types, (a) and (b) are used for pouch cells. (c) is used for cylindrical cells, and (d) is used for prismatic cells. Image credit [13]. (e) Pouch cell showing anisotropic thermal conductivity due to its layered structure and equation for thermal resistance, R_{th} for cross-plane heat transfer showing the location of A and L .

To enhance battery thermal management, certain battery thermal management system (BTMS) needs must be addressed. These include increased heat removal rates [11], reduced battery temperature gradients [11], faster thermal response [4], lower energy consumption [4], lower complexity BTMS design [4], size and weight reduction [4], lower cost [4] and potentially a fundamentally new approach.

Lithium-ion cells consist of layers including the cathode, anode, and separator, as illustrated in Fig. 2. These layers are typically arranged in either a stacked or rolled configuration before being enclosed in a casing that contains the electrolyte. The casing is often constructed from metal, and the common shapes for these casings include cylindrical, prismatic (rectangular cuboid), or pouch formats.

The layered battery cell construction shown in Fig. 2a through d and in Fig. 2e gives battery cells their anisotropic thermal conductivity property. Heat transfer perpendicular to the layers of battery materials such as copper cathode, aluminum anode, electrolyte, polymer separators and their associated interfacial contact resistances is referred to herein as “cross-plane” heat transfer. And heat transfer parallel to these layers is referred to herein as “in-plane” heat transfer. Due to these many interfacial contact resistances and low thermal conductivity polymer layers, bulk average thermal conductivity in the cross-plane direction is known to be more than an order of magnitude lower than in-plane bulk average thermal conductivity. For example, cross-plane thermal conductivity of a prismatic lithium-ion battery cell is 0.95 W(m K)^{-1} , while in-plane thermal conductivity is 30.8 W(m K)^{-1} [12].

1.1. Gap analysis — strategies for enhancing battery thermal management performance

From a thermal–electrical analogy perspective, the heat removal

rate from a battery can be mathematically described by the equation: $\dot{Q}_{batt} = \Delta T_{batt} / R_{th\ batt}$ as illustrated in Fig. 3a. This equation reveals two primary methods for enhancing the heat removal rate from the battery: increasing the temperature difference, ΔT_{batt} , or reducing the battery's thermal resistance, $R_{th\ batt}$. Historically, the most common approach to battery thermal management has been to focus on increasing ΔT_{batt} .

To achieve a higher $\Delta T_{batt} = T_1 - T_2$ while keeping T_1 at its optimal value, T_2 must be reduced (cooled). Eq. (1) shows two main ways to achieve this. The first method is to increase the heat transfer coefficient, h_{batt} , at the battery surface or to increase the contact area, A_{batt} , over which h_{batt} is acting. The second method involves improving the overall heat transfer coefficient of the radiator or condenser, U_{rad} , or increasing its fin surface area, $A_{rad\ fins}$. However, the second method typically has a smaller impact because the thermal resistance of the radiator is already low due to its large fin area.

$$T_2 = T_{ambient} + \dot{Q}_{batt} \left(\frac{1}{h_{batt} A_{batt}} + \frac{1}{U_{rad} A_{rad\ fins}} \right) \quad (1)$$

Historically, various methods have been employed to increase the heat transfer coefficient, h_{batt} , to achieve a greater temperature differential, ΔT_{batt} . These methods include natural convection [15], forced air cooling [16], pumped single-phase liquid [5], vapor compression refrigeration [17], dielectric fluid immersion [18], pumped two-phase fluid [19], and jet impingement [6].

The increased ΔT_{batt} (higher h_{batt}) approach has its limitations. The United States Advanced Battery Consortium (USABC) advises keeping ΔT_{batt} to no more than 3°C [20]. And increased ΔT_{batt} is known to increase battery degradation [21,22]. Furthermore, with ΔT_{batt} constrained; the heat transfer rate from the battery is limited by $\dot{Q}_{batt} =$

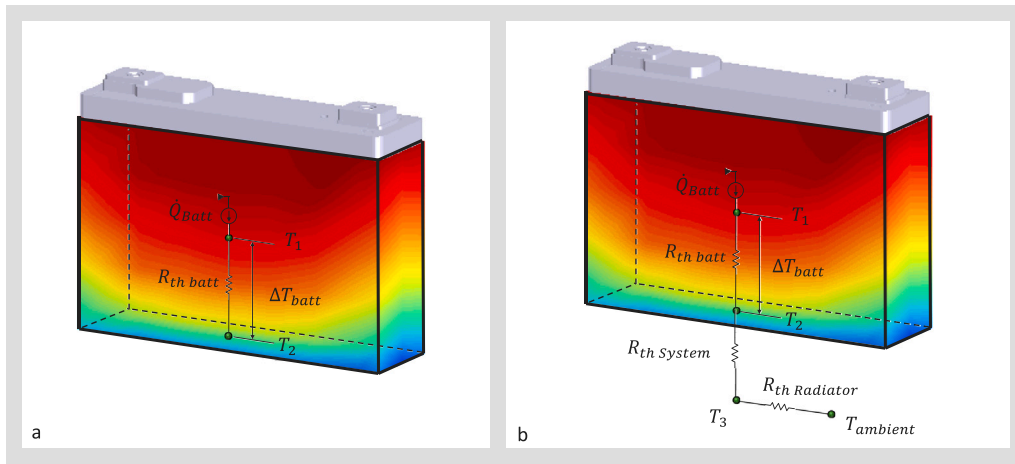


Fig. 3. Prismatic can battery showing equivalent resistance electrical-thermal analogy model.(a) for the battery alone (b) adding a cooling system.
Source: CC-BY image modified from [14].

$\Delta T_{batt}/R_{th}$. As a result, any strategies aimed at enhancing h_{batt} or A_{batt} to subsequently increase ΔT_{batt} become largely similar in terms of heat removal rate.

In contrast to the increased ΔT_{batt} approach, the research herein focuses on reducing $R_{th batt}$. The thermal resistance of a three-dimensional rectangular cuboid, such as certain battery formats, is defined by the equation $R_{th batt} = L/kA$. As illustrated in Fig. 2e, L represents the battery's thickness in the direction of heat transfer, while A is the area perpendicular to the direction of heat flow.

Typically, batteries rely on the lower thermal conductivity of the cross-plane heat transfer path to dissipate heat. In this approach, L is minimized, and A is maximized to reduce $R_{th batt}$. More recently, electric vehicles using pouch cells have adopted battery edge cooling, where the smaller edge, rather than the larger face of the pouch cell, is interfaced with a cooling plate heat exchanger. This configuration transfers heat through the higher thermal conductivity in-plane direction. Research comparing the thermal performance of high k in-plane thermal management to cross-plane methods [22] has revealed several significant advantages of in-plane methods, including a sevenfold reduction in capacity loss, a 66% reduction in costs, and a threefold increase in battery life. However, these studies did not address the impact of reducing the battery's thermal resistance, and as the current needs of battery thermal management show, these methods have not yet achieved the desired results.

To summarize, current batteries optimize L and A to reduce $R_{th batt}$ by utilizing low k cross-plane heat transfer. Some applications have explored edge cooling and tab cooling to investigate the effects of high k in-plane heat transfer. However, no studies have focused on the simultaneous optimization of L and A for a battery using the high k in-plane heat path to reduce $R_{th batt}$ and, in turn, increase \dot{Q}_{batt} .

This work is novel in its approach by addressing this gap and focusing on the combined optimization of L and A with high k in-plane heat transfer to directly reduce thermal resistance and improve battery thermal performance.

1.2. Research objective

The aim of this work is to quantify, the effect on \dot{Q}_{batt} of employing optimized L and A (Optimized aspect ratio) for a battery that takes advantage of high- k in-plane heat transfer. The cell format for this study is a prismatic can cell. The in-plane heat transfer for this work is enabled by a novel and mass-producible heat transfer design shown in Fig. 4. This design is specifically engineered to maximize heat transfer, differentiating it from conventional in-plane cooling methods like tab or edge cooling, which are essentially new applications of existing

battery technologies. Batteries utilizing this advanced heat transfer design will be designated as high-heat transfer (HHT) batteries. HHT batteries also recognized under the trademark ParaThermic® battery technology [23].

1.3. HHT battery design & assembly procedure

Although Fig. 4 is designed to illustrate the HHT battery technology, it is helpful to first understand the assembly process of conventional battery technology. The process begins with Fig. 4a, which shows a prismatic battery cell without its case. In this stage, the current collectors are shown arranged, trimmed, and compressed at each end of the battery cell. For the time being, we will set aside the steps depicted in Fig. 4b through d. Moving on, the next step in the conventional battery assembly, shown in Fig. 4e and f, involves sliding the terminal assembly over the current collectors and ultrasonically welding it in place. Once the weld is complete, the battery and terminal assembly, (excluding the thermal connectors, for now), are inserted into the battery case, as shown in Fig. 4g. Finally, the lid is laser-welded to the battery case. In contrast to this conventional battery, the assembly process for the HHT battery will now be discussed.

The process for the HHT battery again begins with a prismatic battery cell format depicted in Fig. 4a as previously discussed. An extruded aluminum “thermal connector”, also identified by the trademark ThermalConnect® is presented in Fig. 4b. These thermal connectors are ultrasonically welded to one or both of the compressed current collectors illustrated in Fig. 4a, creating a very low thermal resistance conduction heat path to the thermal connector from the battery cell. While the connectors have an ideal design, they have not yet been mathematically optimized for minimal material use or maximum heat transfer. The thermal connectors are coated with a dielectric layer engineered for high adhesion and wear resistance. Although the connectors are stationary and not subject to wear, the coating is well-suited for demanding applications such as engine components and other mechanical parts. This characteristic suggests that the connectors offer greater durability than current battery edge cooling designs, particularly in preventing short circuits. The images in Fig. 4c and d show the battery cell after the thermal connectors have been added. These connectors are designed to create a conduction heat transfer pathway with minimal thermal resistance, efficiently directing heat from the battery's in-plane heat transfer layers to the battery case. The thermal connectors effectively bridge the thermal gap that would exist in a conventional battery that is lacking such thermal connectors. The connectors occupy the space that is empty in the conventional battery, therefore the energy density of the HHT cell remains unaffected. Fig.

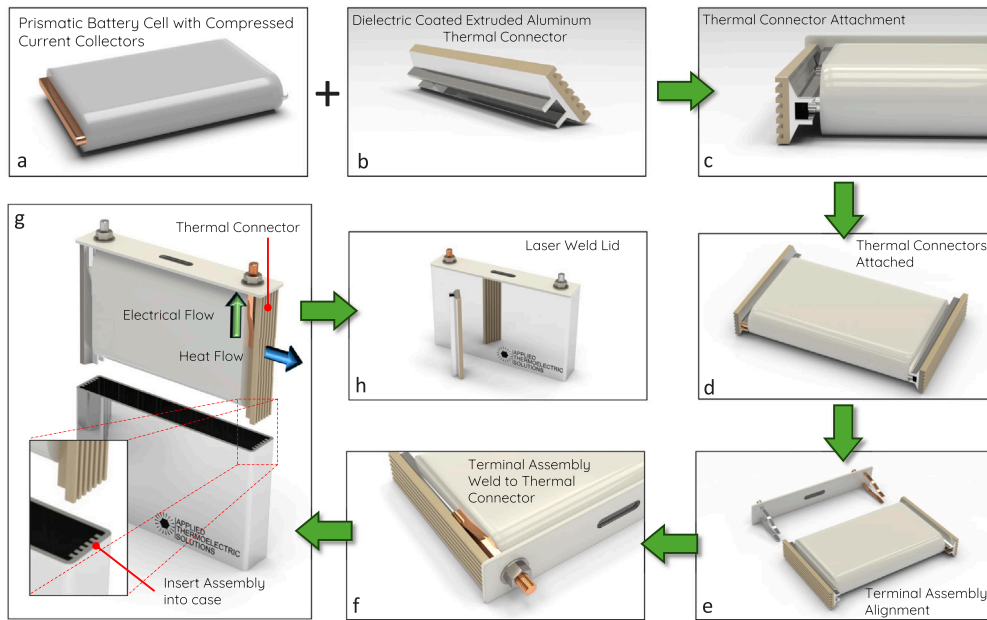


Fig. 4. HHT battery design elements and assembly steps (a) Prismatic battery cell with compressed and trimmed current collectors (b) Extruded aluminum “thermal connector” with dielectric coating (c) Thermal connectors ultrasonically or laser welded compressed current collectors close up view (d) Both thermal connectors attached (e) Electrical terminal assembly alignment (f) Ultrasonic weld terminal assembly to thermal connector non-coated portion (g) Lower cell, thermal and electrical assembly into case (h) Laser weld lid to case.

4e shows the alignment of the electrical terminal assembly with the battery, while Fig. 4f illustrates the terminal assembly being positioned over the thermal connectors, where it is affixed to the non-electrically insulated portion through a method such as ultrasonic welding. Once the thermal connectors and terminal assembly are secured, the battery sub-assembly is placed into the battery case, as depicted in Fig. 4g, with a thin layer of thermal interface material applied between the case and thermal connectors to enhance heat transfer. Finally, to complete the assembly, the lid shown in Fig. 4h is laser welded to the battery case, effectively sealing the cell.

HHT technology sets itself apart from other in-plane heat transfer methods, such as edge cooling or tab/terminal cooling, with its innovative engineered design and a specific emphasis on enhanced thermal performance. By leveraging in-plane heat transfer, HHT allows for optimized battery cell geometry that significantly reduces battery thermal resistance, achieving greater efficiency than is possible with optimized cross-plane geometry due to the high thermal conductivity in the in-plane direction. Thermal resistances in the components are minimized by reducing the thickness of low thermal conductivity coating layer. Interfacial contact resistances are further minimized by maximizing contact area and ensuring metal-to-metal contact. When applied to prismatic can cells, this design transforms the thermal gap within the cell into a thermal bridge, enabling heat to flow freely to the case surface, where it can be effectively dissipated by the thermal management system.

In this context, HHT technology is applied to prismatic cells. When used with pouch cells, an added benefit is the formation of a rigid thermal interface between the battery cell and the heat exchanger. This reduces the need for thick thermal interface material and could enhance heat transfer compared to the flexible interface found in edge cooling.

2. Methods

2.1. Modeling overview

A steady-state equivalent resistance electrical-thermal analogy model (Fig. 5b) is developed for a conventional prismatic battery. The target conventional battery studied herein is a 25 Ah automotive

battery cell by SANYO PANASONIC (Fig. 5a). This is a lithium-ion cell with nickel-manganese-cobalt (NMC)/graphite chemistry [24].

The conventional battery equivalent circuit model is solved symbolically for voltages which are equivalent and analogous to temperatures. The resultant center and surface temperatures are compared and validated against the results of an experiment and model available in the literature [24] with excellent agreement.

A detailed resistive circuit, representing the thermal connector technology and other associated thermal resistances, is incorporated into the validated conventional model to develop the HHT battery model.

To compare the thermal performance of the conventional and HHT batteries, each resistance in the equivalent resistance circuit is modeled as a function of the battery's aspect ratio. This approach enables the calculation of thermal performance across a range of aspect ratios for both conventional and HHT battery types, while maintaining a constant internal case volume.

Boundary conditions applied are base cooling (face 3, Fig. 5b) for the conventional battery and cooling two sides (face 5 and face 6, Fig. 5b) for the HHT battery. Base cooling thermal resistance for forced air, flowing liquid, refrigerant and constant temperature are modeled. Battery performance (temperatures and maximum heat removal rate) for both conventional and HHT batteries are compared under various heat transfer coefficient boundary conditions under variable heat load for a range of battery aspect ratios. Side cooling is selected for the HHT battery because it minimizes the thermal resistance path and provides superior thermal performance. For the conventional battery, base cooling is chosen due to its widespread use and recognition as a standard method for cooling prismatic cells, which allows for a meaningful comparison with the HHT battery that is likely to be familiar to a broad audience.

Eq. (2) defines the thermal resistance for many of the resistors modeled in Fig. 5b and will be referenced herein frequently.

$$R_{th} = \frac{L_{heat\ transfer}}{kA_{heat\ transfer}} \quad (2)$$

Here L is equal to the length of heat transfer conduction in a specific battery component, k is equal to bulk average thermal conductivity of the component in the direction of heat transfer and A is equal to the heat transfer area perpendicular to the direction of heat flow.

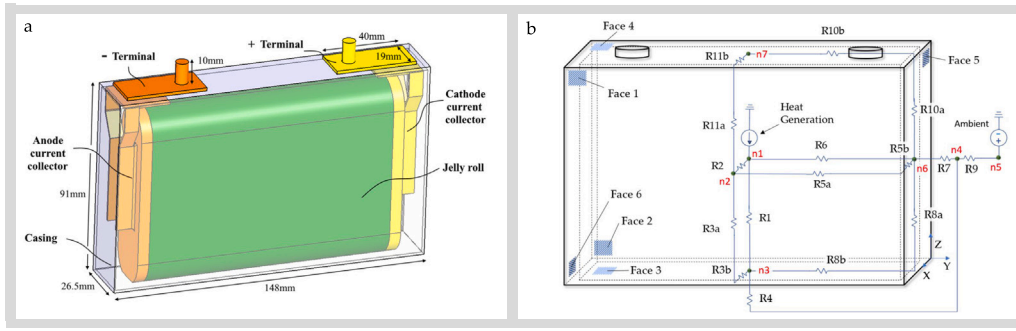


Fig. 5. (a) Target battery cell for modeling. 25 Ah automotive battery cell by SANYO PANASONIC. A lithium-ion cell with nickel-manganese-cobalt (NMC)/graphite chemistry. Image credit [24] (b) Electrical-thermal analogy model of a HHT battery. The model represents target conventional battery upon removal of R6.

2.2. Equivalent resistance model

Equivalent resistance modeling, or electrical/thermal analogy modeling, was chosen for the thermal model because it is known for its speed and accuracy in simulating thermal behavior, allowing for efficient analysis of temperature within the battery. [25]. Fig. 5b is an image of the equivalent resistance electrical-thermal analogy model for the HHT battery. Upon removal of R6, this model represents the conventional battery thermal behavior. With this equivalent circuit model, electrical resistances are equivalent to thermal resistances. The current source at the center of the battery is equivalent to uniform heat generation in the battery and the voltage source is equal to the ambient temperature. Node voltages are equivalent to temperatures.

To reduce the computational power required to solve for the node voltages in the equivalent circuit model and to further increase the speed, the number of nodes and resistors is minimized. This is achieved by applying geometric symmetry, which allows parallel or series resistors to be simplified into a single equivalent resistance wherever possible.

The nodes $n1$ through $n6$ of the model in Fig. 5b represent the temperatures at various locations. For example, $n1$ is the temperature at the center of the battery cell, $n2$ is the temperature of the internal center of aluminum case face 1, $n3$ is the internal temperature at the center of case face 3, $n4$ is the temperature between the battery side heat exchanger and a vehicle side radiator, $n5$ is the ambient temperature, $n6$ is the internal temperature of the battery case face 5 and $n7$ is the internal temperature of the case in face 4 at the top of the battery.

Each of the resistances shown in Fig. 5b represents a thermal resistance. These thermal resistances are the resistance of the battery cell, battery case, thermal connectors, electrolyte, film wrap, cooling method boundary condition or heat exchanger.

Since the thermal resistances are known based on geometry and material properties, the circuit must be solved for the node point voltages/temperatures. To accomplish this, two main software tools were used. Specifically, Symbolic Circuit Analysis in MATLAB® (SCAM tool) [26]. The process of using the SCAM tool is to first draw the circuit using a Simulation Program with Integrated Circuit Emphasis (SPICE) software. After the circuit is drawn, the SPICE program is used to output a netlist. The netlist is a file that contains all the electronic components of the circuit, the nodes and how the circuit is connected. The netlist is an input to the SCAM tool. The SCAM tool then solves the circuit symbolically for the node voltages. The output of the SCAM tool is a list of equations for each node voltage. These node voltages are dependent on the resistances (thermal resistances) in the circuit, the current source (heat generation) and voltage source (ambient temperature).

2.3. Determination of each thermal resistance

To facilitate the recreation of the model and ensure reproducibility of the work, the following sections provide a detailed description of how each thermal resistance in the circuit of Fig. 5b is modeled, along with the assumptions made.

2.3.1.

R1 is the sum of z -axis resistances through the battery cell and case. These resistances R1a through R1e are shown in detail in Fig. 6a and include the cell rectangular cuboid portion, cell rounded bottom half cylinder portion, cell film wrap, cell electrolyte and half of the battery case.

$$R1 = R1a + R1b + R1c + R1d + R1e \quad (3)$$

R1a, is the in-plane thermal resistance of the battery cell for the portion of the cell shaped like a rectangular cuboid. To model the thermal resistance R1a, Eq. (2) is utilized. The heat transfer length for Eq. (2) is equal to $H'/2$ where $H' = H - T$, as defined in Fig. 6a. The heat transfer area for Eq. (2) is equal to $L \times T'$. Thermal conductivity, k_1 is of the cell in this direction is in-plane heat flow.

$$R1a = \frac{\frac{H'}{2}}{k_1 (L \times T')} \quad (4)$$

R1b, is the thermal resistance of the semicircle cross-section geometry rounded cell bottom in Fig. 6a. Or in 3D, the half cylinder in Fig. 7b. The radius of the semicircle is $r_1 = T/2 - \epsilon$.

The battery is wrapped in an acrylic film with thickness, ϵ . The semi-circle cross-section cell bottom consists of battery layers extending radially per Fig. 2d. The thermal conductivity of the layers in-plane and axially is 30.8 W(mK)^{-1} [12] and thermal conductivity cross-plane through the layers is 0.95 W(mK)^{-1} [12].

All of the thermal resistances in this section were solved analytically, except for R1b. Due to the complex geometry of the layered battery structure and the way the layers are wound into the “jelly roll”, CFD analysis was used to calculate R1b. Specifically, STAR-CCM+ is used to model the thermal resistance of semi-circle cross-section portion of the battery cell. This is shown in the CFD model of Fig. 7b. Here a constant thermal heat flux of $Q = 2018 \text{ Wm}^{-2}$ is applied to the large flat surface of the half-cylinder geometry. This is equivalent to 6 W spread evenly across the surface of the rectangular battery cell cross-section. This is a realistic value [24], however, since the simulation is determining thermal resistance in K/W , and the K is proportional to W , any value for W could be used. A constant temperature $T_2 = 25^\circ\text{C}$ is applied to the full rounded portion of the half cylinder. The two small semicircles at each end are considered adiabatic. The resultant average temperature of the top flat surface in combination with the constant average temperature rounded surface are used to calculate ΔT . The heat flux Q and area of the flat surface, $(2r_1)(L)$ is used to calculate \dot{Q} . T_1 is the average resultant flat side temperature that is 33.4°C . Finally, the thermal resistance is calculated using Eq. (5).

$$\text{Thermal Resistance} = \frac{\Delta T}{\dot{Q}} = \frac{T_1 - T_2}{2QLr_1} \quad (5)$$

For the target and validation condition, L is equal to 123 mm and r_1 is per Table 1. This thermal resistance of Eq. (5) in KW^{-1} is modeled for

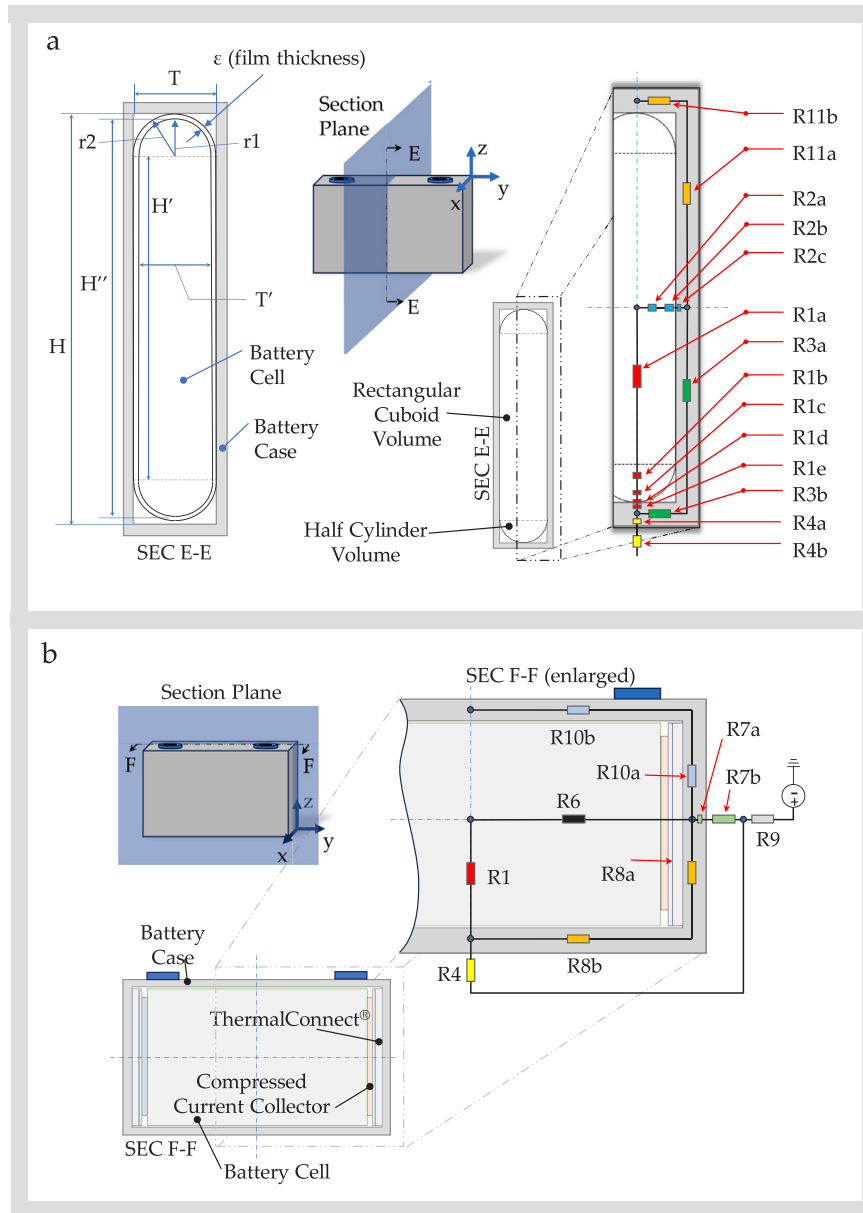


Fig. 6. (a) z-x plane section cut view of battery cell thermal resistances and dimensions for thermal resistance models. (b) z-y plane section cut view of battery cell thermal.

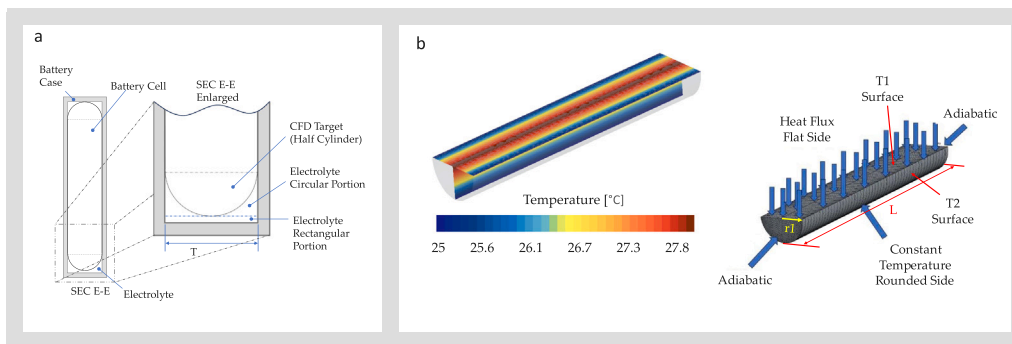


Fig. 7. (a) Battery section view with enlarged image showing electrolyte area broken down into a rectangular portion and a circular portion for thermal resistance calculation as well as section view of CFD target semicircular portion. (b) Battery semicircle cross-section bottom CFD analysis boundary conditions and resultant temperature distribution.

Table 1
Property values and dimensions used in simulations.

Characteristic	Item	Symbol	Value	Source
Thermal conductivity [W/m K]	In-plane cell	k_1	30.8	Lundgren et al. [12]
	Acrylic film	k_2	0.18	Lundgren et al. [12]
	Electrolyte	k_3	0.6	Kleiner et al. [24]
	Aluminum	k_4	238	Lundgren et al. [12]
	Cross-plane cell	k_5	0.95	Lundgren et al. [12]
	Copper-aluminum average	k_6	319	[12]
	Dielectric coating	k_7	2.5	Proprietary
	Thermal paste	k_8	4.4	[27]
Thickness [m]	Electrolyte	ρ	4.0×10^{-4}	[24]
	Dielectric coating	ν	2.0×10^{-5}	Proprietary
	Thermal paste	σ	5.08×10^{-5}	None
	Acrylic film	ϵ	3.5×10^{-4}	Lundgren et al. [12]
Interfacial resistance [W/m K]	Thermal paste	λ	6.3×10^{-6}	Narumanchi et al. [27]
	Thermal connector to current collector	γ	2.0×10^{-5}	Narumanchi et al. [27]
Multiplier [%]	Thermal Connector contact to case area		150	
	Thermal connector width (% of battery thickness)		8.5	
	Collector thickness (% of cell thickness)		24	
	Collector length (% of current collector thickness)		109	
Volume [m ³]	Rectangular cuboid around cell (not case volume)	V	2.2278×10^{-4}	Lundgren et al. [12]
Aspect ratio	Target cell height-to-length	H/L	0.6544	Lundgren et al. [12]
	Target cell thickness-to-length	T/L	0.1829	Lundgren et al. [12]
Cell and case dimensions [m]	Cell thickness with acrylic film	T	0.0225	Lundgren et al. [12]
	Cell thickness without acrylic film	T'	0.0218	Lundgren et al. [12]
	Cell height with rounded ends and acrylic film	H	0.0805	Lundgren et al. [12]
	Cell height without rounded ends	H'	0.058	Calculated
	Cell height without acrylic film	H''	0.0798	Calculated
	Cell length	L	0.123	Lundgren et al. [12]
	Case inner length	L'	0.144	Lundgren et al. [12]
	Case material thickness	β	0.0001	Lundgren et al. [12]
	Radius of battery rounded end without acrylic film	r_1	0.0109	Calculated
	Radius of battery rounded end with acrylic film	r_2	0.01125	Calculated

several combinations of L and r_1 then fitted with an exponential curve fitter. The result of the fit is Eq. (6). The fit has an R^2 value equal to one.

$$R1b = 169.506L^{-1} \quad (6)$$

Eq. (6) is developed with dimensions between 16 and 600 mm and the input for L needs to be in millimeters. The thermal resistance of Eq. (6) is only a function of length (L). This is because in Eq. (5) ΔT scales exactly proportional to r_1 , so those terms along with Q are essentially constants

$R1c$ is the cell film wrap. The battery cell is wrapped with a film that adds thermal resistance to $R1$. The thermal resistance of the film is calculated with Eq. (2). Heat transfer length for Eq. (2) is the thickness of the film, ϵ . Heat transfer area for Eq. (2) is the area calculated by the circumference of the half circle with radius r_1 times the cell length, L . This is $\frac{2\pi r_1}{2} \times L$. Thermal conductivity of the film is k_2 . Using Eq. (2), the thermal resistance of $R1c$ is:

$$R1c = \frac{\epsilon}{k_2 \left(\frac{2\pi r_1}{2} \times L \right)} \quad (7)$$

$R1d$ is the thermal resistance of the rest electrolyte in the bottom of the cell. The electrolyte volume in the cell was measured [24] and contained enough volume to completely fill the electrolyte area shown in Fig. 7a. To model the thermal resistance, the electrolyte is treated as a solid body with no convection per [24] with properties shown Table 1. For simplicity, the electrolyte area is broken down into two portions geometrically. One is a semicircular cross-section portion and one a rectangular cross-sectional portion. The rectangular portion has a heat transfer length for Eq. (2) in the z -direction of ρ which is the distance between the bottom semicircular rounded bottom portion of the cell and the battery case. The heat transfer area for Eq. (2) for the rectangular electrolyte portion is found as $T \times L$.

$$R_{rectangle} = \frac{\rho}{k_3 (T \times L)} \quad (8)$$

To find the thermal resistance of the semi-circular electrolyte portion, the heat transfer length is found by averaging the height of electrolyte using Eq. (8).

$$\text{Electrolyte Rounded Portion Height}_{Average} = \frac{1}{8} (4 - \pi) T \quad (9)$$

With a heat transfer area for Eq. (2) equal to $T \times L$, the result is Eq. (10). Here k_3 is the electrolyte thermal conductivity.

$$\text{Electrolyte Thermal Resistance}_{Rounded Portion} = \frac{\frac{1}{8} (4 - \pi) T}{k_3 L T} = \frac{\frac{1}{2} - \frac{\pi}{8}}{k_3 L} \quad (10)$$

Finally, the equation for $R1d$ is as follows:

$$R1d = \frac{\rho}{k_3 (T \times L)} + \frac{\frac{1}{2} - \frac{\pi}{8}}{k_3 L} \quad (11)$$

$R1e$ is the thermal resistance in face 3 of the battery case in the z -axis direction. This resistance is the computed with Eq. (2). The heat transfer length is half the thickness of the battery case, $\beta/2$. The heat transfer area is $(T)(L')$, and thermal conductivity for the aluminum case is k_4 .

$$R1e = \frac{\beta/2}{k_4 (T L')} \quad (12)$$

2.3.2.

$R2$ of Fig. 5b is the summation of $R2a$ (cell cross-plane), $R2b$ (film wrap) and $R2c$ (case) shown in Fig. 6a. $R2a$ is the thermal resistance of the battery cell in the x -direction which is cross-plane to the layers in the battery cell. The one half is added because $R2$ is the equivalent resistance of two parallel resistances but one is being used due to symmetry

$$R2 = \frac{1}{2} (R2a + R2b + R2c) \quad (13)$$

R2a is the cell cross-plane thermal resistance in the x -direction for the portion of the cell that is the shape of a rectangular cuboid. The heat transfer length in the x -direction is equal to $\frac{T}{2} - \epsilon$. The heat transfer area for Eq. (2) is equal to $L \times H'$. Here $H' = H - T$. Thermal conductivity for Eq. (2) in the cross-plane direction is k_5 .

$$R2a = \frac{\frac{T}{2} - \epsilon}{k_5 (L \times H')} \quad (14)$$

The acrylic film wrap (R2b) adds additional thermal resistance to the R2. The heat transfer length for R2b is ϵ , the film thickness. The heat transfer area for Eq. (2) is equal to $H' \times L$. Thermal conductivity of the acrylic film is, k_2 . With Eq. (2), R2b is:

$$R2b = \frac{\epsilon}{k_2 (H' \times L)} \quad (15)$$

R2c is the thermal resistance into face 1 of the battery case in the x -direction. The heat transfer length for Eq. (2) is half the material thickness of the aluminum battery case which is $\beta/2$. The heat transfer area is equal to $H' \times L$. And thermal conductivity for aluminum, k_4 .

$$R2c = \frac{\beta/2}{k_4 (H' \times L)} \quad (16)$$

2.3.3.

R3 consists of two resistors R3a and R3b that model the thermal resistance of the battery case. These two are connected electrically in series. R3a is located in face 1 running in the z -direction and R3b is in face 3 running in the x -direction. The $1/2$ is added due to model symmetry simplification.

$$R3 = \frac{1}{2} (R3a + R3b) \quad (17)$$

R3a is the thermal resistance in the z -direction in Face 1 of the aluminum battery case. Eq. (2) is used to model the thermal resistance of R3a. The heat transfer length is $H'/2 + \beta/2$. The heat transfer area for Eq. (2) is $(L' + 2\beta) \times \beta$. Thermal conductivity of aluminum is k_4 . With these, thermal resistance is Eq. (18).

$$R3a = \frac{\frac{H}{2} + \frac{\beta}{2}}{k_4 ((L' + 2\beta) \times \beta)} \quad (18)$$

R3b is the thermal resistance in face 3 of the battery case in the z -direction. To model R3b, Eq. (2) is utilized. The heat transfer length for R3b is $T/2 + \beta/2$. The heat transfer area is $(L' + 2\beta) \times \beta$, thermal conductivity of aluminum is k_4 . With these, thermal resistance, R3b is Eq. (19).

$$R3b = \frac{\frac{T}{2} + \frac{\beta}{2}}{k_4 ((L' + 2\beta) \times \beta)} \quad (19)$$

2.3.4.

R4 of Figs. 5b and 7b consists of two resistors in series, R4a and R4b. These consist of the face 3 bottom of case in the z -direction and the cooling method resistance/boundary conditions. R4b is only used for the conventional battery cooling model except for the target battery conventional modeling validation condition which is a constant temperature boundary condition and therefore R4 is equal to zero. The other boundary conditions used for R4 are forced convection with air, forced liquid cooling and refrigerant cooling. For forced air, it is assumed the air acted directly on the battery cell. For liquid and refrigerant, the same assumption is made as the heat exchanger thermal resistance is known to be very small [24].

$$R4 = R4a + R4b \quad (20)$$

R4a is the thermal resistance in face 3 which is the bottom of the case in the z -direction. To model R4a, Eq. (2) is utilized. The heat transfer length for R4a is $\beta/2$. The heat transfer area for Eq. (2) is

$(T + 2\beta) \times (L' + 2\beta)$. Thermal conductivity of aluminum is k_4 . With this, Eq. (2) is:

$$R4a = \frac{\frac{\beta}{2}}{k_4 ((T + 2\beta) \times (L' + 2\beta))} \quad (21)$$

R4b is the convection boundary thermal resistance and is modeled using Eq. (22). Here h is the heat transfer coefficient and A is the area the heat transfer coefficient is acting upon. For R4a, the area is the bottom of the battery case is $(T + 2\beta) \times (L' + 2\beta)$.

$$R4b = \frac{1}{hA} = \frac{1}{h ((T + 2\beta) \times (L' + 2\beta))} \quad (22)$$

The heat transfer coefficient for forced air is 25 W/m²K-1 [28], 390 W/m²K-1, [28] for liquid cooling and 1740 W/m²K-1 [29,30] for refrigerant.

2.3.5.

R5 is the sum of thermal resistances R5a and R5b in the aluminum battery case. R5a is located in face 1 of the aluminum battery case in the y -direction. And R5b face 5 in the x -direction. The $1/4$ in Eq. (23) below is added due to model symmetry which uses the equivalence law of parallel resistors of equal value.

$$R5 = \frac{1}{4} (R5a + R5b) \quad (23)$$

R5a is the thermal resistance in the case, face 1 in the y -direction. To model R5a, Eq. (2) is utilized. The heat transfer length for Eq. (2) is $L'/2 + \beta/2$. The heat transfer area for Eq. (2) is $\beta \times (H + 2\beta)$. The thermal conductivity of aluminum, k_4 is used. Therefore, R5a is:

$$R5a = \frac{L'/2 + \beta/2}{k_4 (\beta \times (H + 2\beta))} \quad (24)$$

R5b is the thermal resistance in face 5 of the battery case in the x -direction. The modeling process for R5b is to again use Eq. (2). The heat transfer length for Eq. (2) is $T/2 + \beta/2$. The heat transfer area is $(H + 2\beta) \times \beta$. Here k_4 is the thermal conductivity of aluminum. The thermal resistance is:

$$R5b = \frac{T/2 + \beta/2}{k_4 ((H + 2\beta) \times \beta)} \quad (25)$$

2.3.6.

R6 captures the thermal resistance of the battery cell in-plane, thermal connector and case resistance. For conventional batteries there is a thermal gap between the battery cell and case and thus no appreciable y -direction heat flow. Therefore, for the conventional model R6 is ∞ . For the HHT model, the modeling of R6 is discussed below.

Section D-D of Fig. 8 shows a cross-section of a prismatic HHT battery. This section shows the x - y plane of the battery cell and case. Thermal resistances are shown drawn through the in-plane direction of the battery cell, uncompressed current collectors, compressed current collector, interfacial resistance between compressed current collector and thermal connector, thermal connector, electrically insulative coating on thermal connector, thermal paste, interfacial thermal resistances, and battery case. The $1/2$ coefficient is added due to symmetry assumptions in the model.

The dimensions shown in Fig. 8 are all scaled from the battery cell thickness T . As T varies in the model, each thermal connector dimension shown scales to keep the thermal connector dimensions proportional to T . For example, the compressed current collector is always 24% of T as T varies. Other dimensions have a second scaling factor; for instance, the dimension $1.09 \times (24\%) \times T$ shows the dimension as 9% of the compressed current collector, which was previously scaled from T .

$$R6 = \frac{1}{2} (R6a + R6b + R6c + R6d + R6e + R6f + R6g + R6h + R6i + R6j + R6k + R6l + R6m) \quad (26)$$

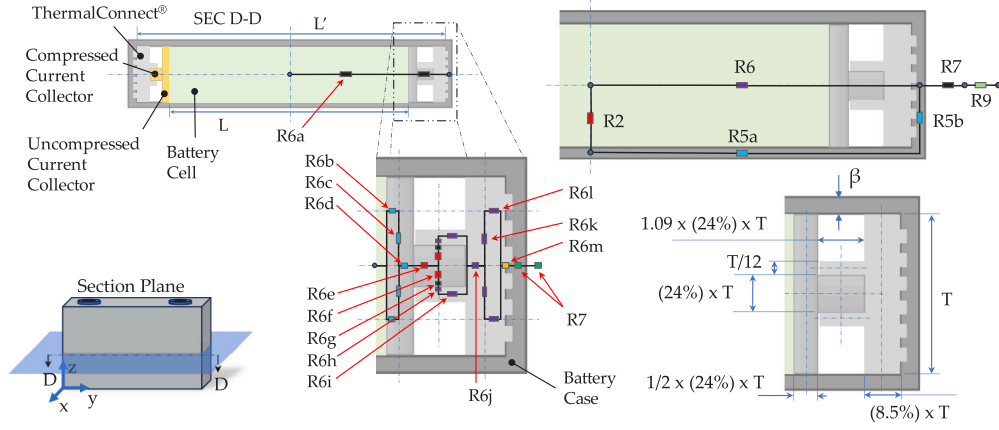


Fig. 8. Section D-D showing R2, R5a, R5b, R6, R7, R9, thermal connector thermal resistances, and dimensions and scaling factors.

R6a is the thermal resistance of the battery cell in-plane in the y -direction of heat flow. For Eq. (2), the heat transfer length is one half of the length of the battery cell or $L/2$. The heat transfer area for Eq. (2) is the summation of the area of two semicircular ends of the battery and the rectangular cuboid center which is $\pi r_1^2 + (H')(T')$. The thermal conductivity is that of the cell in-plane which is k_1 . R6a is:

$$R6a = \frac{L/2}{k_1 (\pi r_1^2 + (H')(T'))} \quad (27)$$

R6b is the thermal resistance of the uncompressed current collector. The heat transfer length for R6b from Fig. 8 is $1/2(1/2 \times 0.24 \times T)$. Here an additional $1/2$ is added outside the parenthesis because the distance is half of the defined distance on the drawing of $(1/2 \times 0.24 \times T)$. The heat transfer area for R6b is $(T \times H)$. Because there are two R6b in parallel, the law of parallel resistors says the equivalent resistance of two equal value resistor is one half the original value. Therefore, an additional $1/2$ is placed in front of the equation for thermal resistance shown in Eq. (28). The thermal conductivity of the compressed current collector will either be aluminum or copper, depending on the side of the battery. Since the principle of symmetry is being use, the thermal resistance model uses an average of the thermal conductivity of aluminum and copper, k_6 .

$$R6b = \left(\frac{1}{2}\right) \left(\frac{\frac{1}{2} \times 0.24 \times T}{k_6 (T \times H)}\right) \quad (28)$$

R6c is the thermal resistance of the uncompressed current collectors. For R6c, the heat transfer length is $(1/4)T$. The heat transfer area is $H(1/2 \times 0.24 \times T)$. Since there is an identical resistor in parallel, thermal resistance using Eq. (2) for R6b becomes Eq. (29). Per the description of R6b, the thermal conductivity is k_6 .

$$R6c = \left(\frac{1}{2}\right) \frac{\left(\frac{1}{4}\right)T}{k_6 \left(H \left(\frac{1}{2} \times 0.24 \times T\right)\right)} \quad (29)$$

R6d is an identical resistance to R6b but is modeled with one resistor rather than two.

$$R6d = R6b \quad (30)$$

R6e is the thermal resistance of the compressed current collector. The heat transfer length for R6e is $1/2(1/2 \times 0.24 \times T)$ per Fig. 8. The heat transfer area for R6e is $(0.24 \times T \times H)$. Along with the uncompressed current collector, the compressed current collector also uses a thermal conductivity that is the average copper and aluminum, k_6 . Using Eq. (2), R6e is:

$$R6e = \frac{1/2(1/2 \times 0.24 \times T)}{k_6 (0.24 \times T \times H)} \quad (31)$$

R6f is the thermal resistance of the x -direction heat flow in the compressed current collector. The heat transfer length for R6f is $1/4(0.24 \times T)$.

The heat transfer area is $H(1/2 \times 0.24 \times T)$. The thermal conductivity is k_6 . R6f has an identical resistance in parallel, and therefore due to the laws of parallel resistors, Eq. (2) is.

$$R6f = \frac{1}{2} \left(\frac{1/4(0.24 \times T)}{k_6 (H(1/2 \times 0.24 \times T))} \right) \quad (32)$$

R6g is the interfacial thermal resistance between thermal connector and the compressed current collector. Although interfacial resistance of an ultrasonic weld may be ideal for this connection between thermal connector and the compressed current collector, there was no reference found for thermal interface resistance for an ultrasonically welded aluminum/aluminum or aluminum/copper. Therefore, the interfacial resistance of a bolted joint is used. Because interfacial resistance for an ultrasonic weld may be lower than a bolted joint, a HHT battery may show increased performance when modeled with an ultrasonic weld. The interfacial area for the joint is equal to $2 \times ((1.09 \times 0.24 \times T)H)$. The factor of two is used because the weld exists on both side of the compressed current collector. Here $\gamma_{interface}$ represents the interfacial resistance in $m^2 K(W)^{-1}$. Thermal resistance is modeled multiplying one over the area times the interfacial resistance which give thermal resistance in KW^{-1} .

$$R6g = \frac{\gamma_{interface}}{2 \times ((1.09 \times 0.24 \times T)H)} \quad (33)$$

R6h is the x -direction thermal resistance in the connector portion of thermal connector. The heat transfer length for R6h is $1/2(T/12)$. The heat transfer area is $(1.09 \times 0.24 \times T)H$. The thermal conductivity is that of aluminum, k_4 . R6h has an identical resistor in parallel, therefore using Eq. (2), the thermal resistance, R6h is:

$$R6h = \left(\frac{1}{2}\right) \frac{1/2(T/12)}{k_4 ((1.09 \times 0.24 \times T)H)} \quad (34)$$

R6i is the y -direction thermal resistance in the connector portion of thermal connector. The heat transfer length of for R6i is $1/2(1.09 \times 0.24 \times T)$. The heat transfer area is $(T/12)H$. The thermal conductivity is that of aluminum, k_4 . There is an identical resistor in parallel with R6i and therefore Eq. (2) is:

$$R6i = \left(\frac{1}{2}\right) \frac{1/2(T/12)}{k_4 ((1.09 \times 0.24 \times T)H)} \quad (35)$$

R6j is the non-connector portion of thermal resistance of thermal connector in the y -direction. The heat transfer length is $1/2(0.085 \times T)$. The heat transfer area is $(T)(H)$. The thermal conductivity is that of aluminum, k_4 . Using Eq. (2), R6j is:

$$R6j = \frac{1/2(0.085 \times T)}{k_4 (T)(H)} \quad (36)$$

R6k is the non-connector portion of thermal resistance of thermal connector in the x -direction. The heat transfer length for Eq. (2) is $1/4(T)$. The heat transfer area for Eq. (2) is $0.0850T \times H$. The thermal conductivity is that of aluminum, k_4 . There is an identical resistor in parallel, so Eq. (2) is:

$$R6k = \frac{1}{2} \left(\frac{1/4(T)}{k_4(0.0850T \times H)} \right) \quad (37)$$

R6l is the second half of the thermal resistance of the non-connector portion of thermal connector in the y -direction. And therefore, it is identical to R6J.

$$R6l = R6j \quad (38)$$

R6m is the thermal resistance of the electrically insulative coating, thermal paste and thermal paste interfacial resistance.

$$R6m = R6m1 + R6m2 + (2)(R6m3) \quad (39)$$

R6m1 is the thermal resistance of the electrically insulative coating. An electrically insulative hard coating is applied to the aluminum thermal connector bar to allow for thermal conduction but prevent an electrical short through the aluminum battery case. For Eq. (2), the heat transfer length for the electrically insulative coating is the thickness of the coating, v . The heat transfer area of the coating is equal to $T \times H \times A_{multiplier}$. $A_{multiplier}$ is an assumption of how much the notched shape multiplies the contact area vs. a purely flat shape. This is left as a variable so it could be studied without modeling complex geometries. The thermal conductivity of the coating is, k_7 . The thermal resistance of R6m1 from Eq. (2) is:

$$R6m1 = \frac{v}{k_7(T \times H \times A_{multiplier})} \quad (40)$$

R6m2 is the thermal resistance of the thermal paste. Thermal paste is used to fill microscopic air gaps between thermal connector and the battery case. This thermal paste is thermally resistive; however, it has a lower thermal resistance than having the microscopic air gaps. The heat transfer length of the thermal paste is the thickness of the paste, σ . The heat transfer area is $T \times H \times A_{multiplier}$. The thermal conductivity is that of the grease is, k_8 .

$$R6m2 = \frac{\sigma}{k_8(T \times H \times A_{multiplier})} \quad (41)$$

R6m3 is the interfacial resistance of the thermal paste. Interfacial thermal resistance exists between the grease layer and thermal connector and between the grease layer and the battery case. The interfacial resistance is symbolized at λ with units of $m^2 K(W)^{-1}$. The contact area is represented by $T \times H \times A_{multiplier}$. Multiplying the interfacial resistance by one over the contact area gives thermal resistance.

$$R6m3 = \frac{\lambda}{(T \times H \times A_{multiplier})} \quad (42)$$

2.3.7.

R7 is the thermal resistance of the case side wall and the cooling method/ boundary condition resistance. R7 is $1/2$ the sum of R7a and R7b. The $1/2$ is due to symmetry in the model and the law of equivalent resistance for two identical value resistors. The R7a heat transfer path is halfway through the battery case on face 5. Symmetry has an identical resistance through face 6. R7b is the thermal resistance due to the heat transfer coefficient on face 5 and face 6. R7 is used only for the HHT model and not the conventional model. The conventional model is base cooled and therefore uses R4. HHT does not use R4.

$$R7 = \frac{1}{2} (R7a + R7b) \quad (43)$$

R7a is the battery case thermal resistance in face 5 in the y -direction. Eq. (2) is used model R7a. The heat transfer length of R7a is

$\beta/2$. The heat transfer area is $(H)(T)$. The case material is aluminum and therefore thermal conductivity is k_4 . Eq. (2) is:

$$R7a = \frac{\beta/2}{k_4((H)(T))} \quad (44)$$

R7b is the thermal resistance of the cooling method at Face 5. Here h is the heat transfer coefficient and A is the area that the heat transfer coefficient is acting upon. For R7b, the area of the battery case is face 5 and is equal to $(T + 2\beta) \times (H + 2\beta)$.

$$R7b = \frac{1}{hA} = \frac{1}{h((T + 2\beta) \times (H + 2\beta))} \quad (45)$$

The heat transfer coefficient for forced air is $25 \text{ W(m}^2 \text{ K)}^{-1}$ [28], $390 \text{ W(m}^2 \text{ K)}^{-1}$, [28] for liquid cooling and $1740 \text{ W(m}^2 \text{ K)}^{-1}$ [29] for refrigerant.

2.3.8.

R8 is the thermal resistance of the battery case in the z and y -dimensions in face 3, 4, 5 and 6. R8 is $1/2$ the sum of R8a and R8b. This $1/2$ is due to this resistance being in two places symmetrically and the law of equivalent parallel resistors.

$$R8 = \frac{1}{2} (R8a + R8b) \quad (46)$$

R8a is the thermal resistance in the battery case face 5 in the z -direction. Eq. (2) is used to model R8a. The heat transfer length for Eq. (2) is $(1/2)H + (1/2)\beta$. The heat transfer area for Eq. (2) is $(T + 2\beta)\beta$. The thermal conductivity is for aluminum, so k_4 is used. Eq. (2) gives:

$$R8a = \frac{(1/2)H + (1/2)\beta}{k_4((T + 2\beta)\beta)} \quad (47)$$

R8b is the thermal resistance of the battery case in face 3 in the y -direction. Eq. (2) is used to model R8b. The heat transfer length for Eq. (2) is $(1/2)L' + (1/2)\beta$. The heat transfer area for Eq. (2) is $(T + 2\beta)\beta$. The thermal conductivity is for aluminum, so k_4 is used. Eq. (2) gives:

$$R8b = \frac{(1/2)L' + (1/2)\beta}{k_4((T + 2\beta)\beta)} \quad (48)$$

2.3.9.

R9 is the thermal resistance of the system radiator or condenser. For R9 a radiator is used for liquid cooling and a condenser is used for refrigerant cooling. For air cooling and constant temperature boundary conditions, there is no system radiator, so $R9 = 0$ for those cases. The convection thermal resistance of a heat exchanger can be modeled as one over the overall heat transfer coefficient h of the heat exchanger times the total heat transfer area heat exchanger.

$$R9 = \frac{1}{hA} \quad (49)$$

For the radiator used, the heat transfer area is 6.05 m^2 and the heat transfer coefficient is $986 \text{ W(m}^2 \text{ K)}^{-1}$ [31]. For the condenser used, the heat transfer area is 7.14 m^2 and the heat transfer coefficient is $4174 \text{ W(m}^2 \text{ K)}^{-1}$ [32]

2.3.10.

R10a is the z -direction thermal resistance of the battery case in face 5 and R10b is the y -direction thermal resistance in face 4. Although these values are not symmetrical to R8a and R8b, the values used are the same.

$$R10a = R8a \quad (50)$$

$$R10b = R8b \quad (51)$$

2.3.11.

R11a is the z -direction thermal resistance of the battery case in face 1 and R11b is the x -direction thermal resistance in face 4. These values are not symmetrical to R3a and R3b, however the values used are the same.

$$R11a = R3a \quad (52)$$

$$R11a = R3a \quad (53)$$

2.4. Boundary conditions

Two sets of model boundary conditions are used in this study: the first set is for validating the base model that represents the conventional target SANYO PANASONIC cell, and the second set is for the simulations conducted after the model validation and used to generate the results section.

For model validation, real battery electric vehicle (Real BEV) boundary conditions, as defined in [24], are used. These boundary conditions simulate a single battery cell within an actual BEV battery pack. The Real BEV conditions include a constant temperature at the cell bottom (face 3 of Fig. 5b, representing base cooling with a liquid heat exchanger that maintains a constant temperature of 30 °C. In a real BEV battery pack, the large cell faces (faces 1 and 2 in Fig. 5b are considered adiabatic, as the target battery is surrounded by other cells, resulting in minimal temperature differences between them. Similarly, faces 4, 5, and 6 in Fig. 5 are treated as adiabatic due to negligible convection and radiation losses in a real BEV.

To facilitate the recreation of the model and results presented here, Table 2 is provided. This table summarizes the thermal resistances for the model that correspond to the target conventional SANYO PANASONIC battery geometry. It also includes a validation column, which uses the same boundary conditions found in the experimental results and model from the literature [24], enabling validation of the model herein.

Table 2 lists values for thermal resistances R1 through R11 that define geometry and boundary condition thermal resistances. R4, R7 and R9 are specifically resistances that define only boundary conditions. As an example, for validation column:

- R4 represents the boundary resistance for the constant temperature condition at the battery bottom and is set to zero for validation. Constant temperature implies no thermal resistance.
- R6 accounts for the in-plane heat path, which does not exist in the target battery, so its value is set to infinity or a large enough number to make heat flow through it negligible.
- R7 represents an adiabatic boundary, where the resistance is set to a sufficiently high value to make heat flow negligible.
- R9 corresponds to another constant temperature boundary condition, so its value is also set to zero.

Additional columns are included for the air, liquid, and refrigerant boundary conditions for both the conventional and HHT batteries, specifying the thermal resistances that define each boundary condition.

For the modeling conditions that generated the results presented here, the boundary conditions are air, liquid, and refrigerant, but the locations of the cooling vary depending on whether the battery is the conventional target or the HHT battery. The conventional battery uses base cooling (face 3) with face 5 being adiabatic, while the HHT battery cools the sides (face 5) with face 3 being adiabatic. Additionally, it is important to note that R9, which represents the radiator, is set to zero for air cooling. This is based on the assumption of direct air cooling, where the hot air is transferred directly to the ambient environment.

2.5. Additional model considerations

For the target battery, with the resistor analogy model developed, thermal resistances calculated, and boundary conditions aligned with the experimental setup from the literature, the model is nearly ready for execution. Once run, its output can be compared with the experimental results, allowing for an assessment of whether the model's accuracy is sufficient to inspire confidence in its predictions. However, a few additional considerations needed to be addressed before proceeding with the model validation.

These considerations mainly arise from the fact that the model presented here is set up for steady-state analysis, while the literature experimental and model results are based on transient temperature vs. time models. The first consideration involved ensuring that the transient temperature data from the literature had reached steady-state before comparing it with the single-point output of the steady-state model.

Another important consideration was the transient heat generation used in the literature. A method had to be developed to average the transient heat generation over time and convert it into a single point value suitable for the steady-state model.

To determine whether the literature experiment and literature model temperatures had reached steady-state, their transient data needed to be verified to have a time constant of at least 5τ .

Using the literature transient temperature data, temperature vs. time is fitted with Eq. (54) to determine the time constant of the literature data. In this equation, T is temperature, t is time, T_0 is the initial temperature, T_f is the final temperature and τ is the time constant. T_f is calculated by averaging the last 22 data points from the transient data in the literature.

$$T(t) = T_f + (T_0 - T_f) e^{\left(-\frac{t}{\tau}\right)} \quad (54)$$

The curve fit of the data described by Eq. (54) is optimized by minimizing the sum of squared differences between the fitted curve and the actual temperature data from both the experiment and the model in the literature. The resulting curve fit yields a time constant of $5\tau = 3642$ s. Since the experimental and model temperature data from the literature extended beyond this value, the transient data is confirmed to have reached a steady-state, with a final surface temperature (T_f) of 37.6 °C. This steady-state temperature is then used as the target value for model validation in this study.

Using the same process applied to the surface temperature above, the battery center temperature in the literature model was also confirmed to have reached steady-state, with a time constant of $5\tau = 3642$ s. A final battery center temperature of 41.1 °C is then used for steady-state target battery model validation herein.

The heat generation data from [24] was provided as a transient plot of heat generation versus time, representing the heat generated during the first cycle of a constant 75-amp charge/discharge cycle (equivalent to 3 times the rated capacity of the 25 Ah battery). The transient heat generation ranged from approximately 8 to 22 W. It is important to note that after each 75-amp charge or discharge, a 10-s rest period was applied during which no heat was generated. This rest period resulted in a 0.55% reduction in the average heat generation. The final averaged heat generation value used for the steady-state model in this study is 12.85 W.

Another consideration was that the experiment had a heat removal rate of 0.85 W through the terminal-connected copper cables. In the model, this is accounted for by reducing the battery's heat generation by 0.85 W. The model is validated against the test run from [24], which did not include a thermal pad between the cell and the cooling source. This approach is considered the most appropriate as it minimizes the number of variables, ensuring that the validation focuses solely on the battery model, rather than a combined thermal pad and battery model.

Table 2

Summary of resistor values and boundary conditions.

Resistances for target 25 Ah automotive battery cell by SANYO PANASONIC								
Resistor	Thermal resistance [kW ⁻¹]	Boundary condition and thermal resistance [kW ⁻¹]						
		Bottom (face 3) - Conventional				Side (face 5) - HHT		
		Validation	Air	Liquid	Refrigerant	Air	Liquid	Refrigerant
R1	3.8864							
R2	0.9406							
R3	0.3777							
R4	varies →	0 [24]	9.8954	0.6349	0.1427	adiab.	adiab.	adiab.
R5	1.0727							
R6	(0.7204) ^a	∞						
R7	varies →	adiab.[24]	adiab.	adiab.	adiab.	11.1831	0.7174	0.1615
R8	4.8555							
R9	varies →	0 [24]	0	1.676 · 10 ⁻⁴	3.355 · 10 ⁻⁵	0	1.676 · 10 ⁻⁴	3.355 · 10 ⁻⁵
R10	4.8555							
R11	0.3777							

^a Not present in model validation for target 25 Ah automotive battery cell by SANYO PANASONIC.**Table 3**

Model compared to published experiment [24].

	Published experiment [24]	Model herein	Temperature delta
Battery surface Temperature [°C] (No Thermal Pad)	36.7	36	0.7

Table 4

Model compared to published model [24].

	Published model [24]	Model herein	Temperature delta
Battery surface Temperature [°C]	37.6	36.4	1.2
Battery center Temperature [°C]	41.1	44.9	-3.8

2.6. Model validation

To validate the model herein, the surface and center temperature results are compared with the literature experiment and model from [24]. This comparison is shown in Tables 3 and 4. Surface temperature delta is within 0.7 °C of the published experiment and 1.2 °C of the published CFD model. The battery center temperature is within 3.8 °C of the published CFD model. For comparison, standard K-type thermocouple error is +/− 2.2 °C or 4.4 °C spread [33], which indicates that the temperature deviations between the models are reasonable. Therefore, we can proceed with confidence in running simulations using the model.

In addition to examining absolute errors, we also considered relative percent errors. When comparing our model to the published experimental data, we observed a 1.9% error in reproducing the battery surface temperature. When comparing our model to the published CFD model, the relative errors were 3.2% for the surface temperature and 9.2% for the battery center temperature. These relative error values of 1.9% for the comparison between the equivalent resistance model and the published experiment, and 3.2%–9.2% for the comparison between the equivalent resistance and CFD models are within a reasonable range, especially considering the simplicity of the equivalent resistance model compared to the detailed CFD simulation. For most practical applications, the equivalent resistance model provides an excellent balance between computational efficiency and accuracy.

2.7. Variable battery aspect ratio modeling

After the model validation, the hypothesis that changing the battery cell aspect ratio could reduce the thermal resistance of the battery

and thus improve heat transfer performance is revisited. To investigate this, thermal resistance models are set up with variables in nested programming for-loops. The model calculated battery thermal resistance, maximum heat removal and battery temperatures for 2500 combinations of battery height to length (H/L) ratio and battery thickness to length (T/L) ratios which ranged from 0.05 to 10.

To remove the variability of changing battery case internal volume, each point is calculated at a constant volume of $2.2278 \times 10^{-4} \text{ m}^3$. This is the volume of the validation target conventional battery cell herein. It should be noted that this volume is not the internal volume of the case, or the volume contained in the external rectangular volume of the battery case. This is the volume of an imaginary rectangular cuboid with length, width and height that contains the active cell portion of the battery. This volume is smaller than the internal case volume.

Constant volume is arrived at using Eq. (55). In Eq. (55), V is equal to the constant volume, H/L is the height to length ratio of the specified volume and T/L is the thickness to length ratio of the specified volume. To determine L from the resultant surface plots, Eq. (55) is used with the specified constant volume in Table 1 and chosen aspect ratio combinations. H and T can then be calculated by $(H/L) \times L$ and $(T/L) \times L$.

$$L = \sqrt[3]{\frac{V}{\left(\frac{H}{L}\right)\left(\frac{T}{L}\right)}} \quad (55)$$

3. Results

3.1. Battery center temperature vs. Aspect ratio

Fig. 9a presents a plot of battery temperature versus the battery height-to-length ratio (H/L), with a constant battery thickness-to-length ratio (T/L) of approximately 5. Here, H and T are defined in Fig. 6, while L is specified in Fig. 8.

Fig. 9b shows a plot of battery temperature versus the T/L ratio, with a constant H/L ratio of approximately 5. Both Fig. 9a and b display the temperature at the center of the battery for both conventional and HHT batteries, under air cooling boundary conditions. These conditions include a heat transfer coefficient of $25 \text{ W(m}^2 \text{ K)}^{-1}$, an ambient temperature of 30 °C , and a battery heat generation of 1.4 W . Both Fig. 9a and b demonstrate that the HHT battery maintains significantly lower temperatures than the conventional battery under the same conditions. However, these plots are limited in that they do not cover the full range of the x -axis, making them appear truncated. Specifically, each plot only shows the relationship between battery temperature and either the T/L ratio at a constant H/L ratio, or the H/L ratio at a constant T/L ratio. As a result, they do not fully capture the interaction between H/L and T/L across their entire ranges. To provide a clearer picture, we chose to present the data in the form of 3D plots,

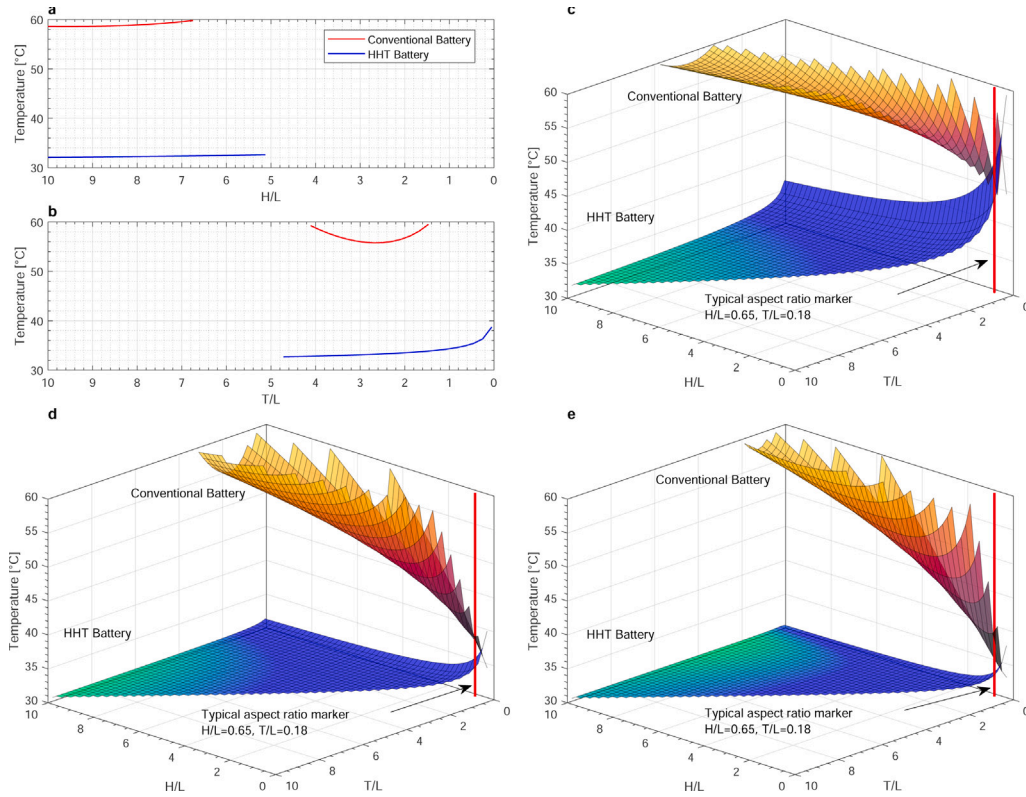


Fig. 9. Battery steady-state center temperature vs. aspect ratio (T/L and H/L) for conventional and HHT batteries with various heat transfer coefficients and heat generation rates. Ambient temperature is $30\text{ }^{\circ}\text{C}$. Conventional batteries use base cooling, while HHT batteries use side cooling. Aspect ratios resulting in battery center temperatures above $60\text{ }^{\circ}\text{C}$ are not shown. (a) Battery steady-state center temperature vs. H/L ratio, with a constant T/L ratio of 5. Heat transfer coefficient is $25\text{ W(m}^2\text{K)}^{-1}$, and battery heat generation is 1.4 W . (b) Battery steady-state center temperature vs. T/L ratio, with a constant H/L ratio of 5. Heat transfer coefficient is $25\text{ W(m}^2\text{K)}^{-1}$, and battery heat generation is 1.4 W . (c) Air cooling with a heat transfer coefficient of $25\text{ W(m}^2\text{K)}^{-1}$, and battery heat generation is 1.4 W . (d) Liquid cooling with a heat transfer coefficient of $390\text{ W(m}^2\text{K)}^{-1}$, and battery heat generation is 4 W . (e) Refrigerant cooling with a heat transfer coefficient of $1740\text{ W(m}^2\text{K)}^{-1}$, and battery heat generation is 6 W .

as shown in Fig. 9c through Fig. 9e, rather than using cross-sectional views of a 3D plot.

Fig. 9c through e present 3D plots of battery cell center temperature as a function of both T/L ratio and H/L ratio. The heat transfer coefficients for the boundary conditions are $25\text{ W(m}^2\text{K)}^{-1}$ in Fig. 9c, $390\text{ W(m}^2\text{K)}^{-1}$ in Fig. 9d, and $1740\text{ W(m}^2\text{K)}^{-1}$ in Fig. 9e. The corresponding heat generation rates are 1.4 , 4 , and 6 W , respectively.

It is notable that only half of the xy -plane contains plotted data points. This is due to the three-dimensional geometry of the prismatic cell, which changes with variations in the height-to-length and thickness-to-length ratios. The prismatic cell is essentially a rectangular cuboid with half-cylinders at both ends. When the thickness-to-length ratio is greater than or equal to the height-to-length ratio, the height of the rectangular cuboid can approach zero, causing the geometry to no longer be prismatic. As the study focuses on prismatic cells, non-prismatic geometries were excluded from the data programmatically.

The first observation from these 3D plots is that, for most combinations of T/L and H/L aspect ratios, the HHT battery center temperature is much lower than the conventional battery center temperature and is much closer to the ambient temperature of $30\text{ }^{\circ}\text{C}$. The maximum temperature limit plotted is $60\text{ }^{\circ}\text{C}$, and many of the conventional battery temperatures exceed this limit, which is why they are not shown.

In each of the three cases, there is a noticeable trend where the best-performing conventional battery aspect ratios are approximately equal to the worst-performing HHT battery aspect ratios. This suggests that the aspect ratio of the conventional cell may already be optimized.

The heat generation rates of 1.4 , 4 , and 6 W were selected somewhat iteratively and subjectively. If the chosen heat generation rate is too

high, many of the conventional battery aspect ratios would exceed $60\text{ }^{\circ}\text{C}$ and therefore would not be shown on the plot, making the conventional battery surface difficult to compare with the HHT surface. Conversely, if the heat generation rate is too low, the full performance potential of the HHT battery could be easily underestimated.

3.2. Maximum heat removal capacity vs. Aspect ratio

Looking at battery temperature is an important way to assess thermal management performance. However, as described above, the 3D temperature plots did not seem like the best way to compare maximum performance of HHT and conventional batteries. To better understand the full capability of both conventional and HHT batteries, the maximum heat removal rate was defined and plotted in Fig. 10a through c.

Fig. 10a through c are plots of maximum battery cell heat removal rate vs. battery aspect ratio. The heat transfer coefficient boundary conditions are 25 , 390 and $1740\text{ W(m}^2\text{K)}^{-1}$ respectively. The heat generation in the figures represents the maximum heat removal rate possible. And this maximum heat transfer rate is defined as a heat removal rate that produces no more than a $60\text{ }^{\circ}\text{C}$ battery center temperature or a ΔT in the cell in the x , y , or z -dimension that does not exceed $20\text{ }^{\circ}\text{C}$ under the stated boundary conditions. This definition represents an extreme condition designed to demonstrate maximum capabilities.

It is notable for Fig. 10a through c, that, at the typical aspect ratio marker, the conventional battery exhibits the maximum heat removal rate. This suggests that prior work may have optimized the conventional battery's aspect ratio for thermal management.

For air and liquid cooling, the maximum heat removal capability approaches an asymptote as the thickness-to-length (T/L) ratio increases.

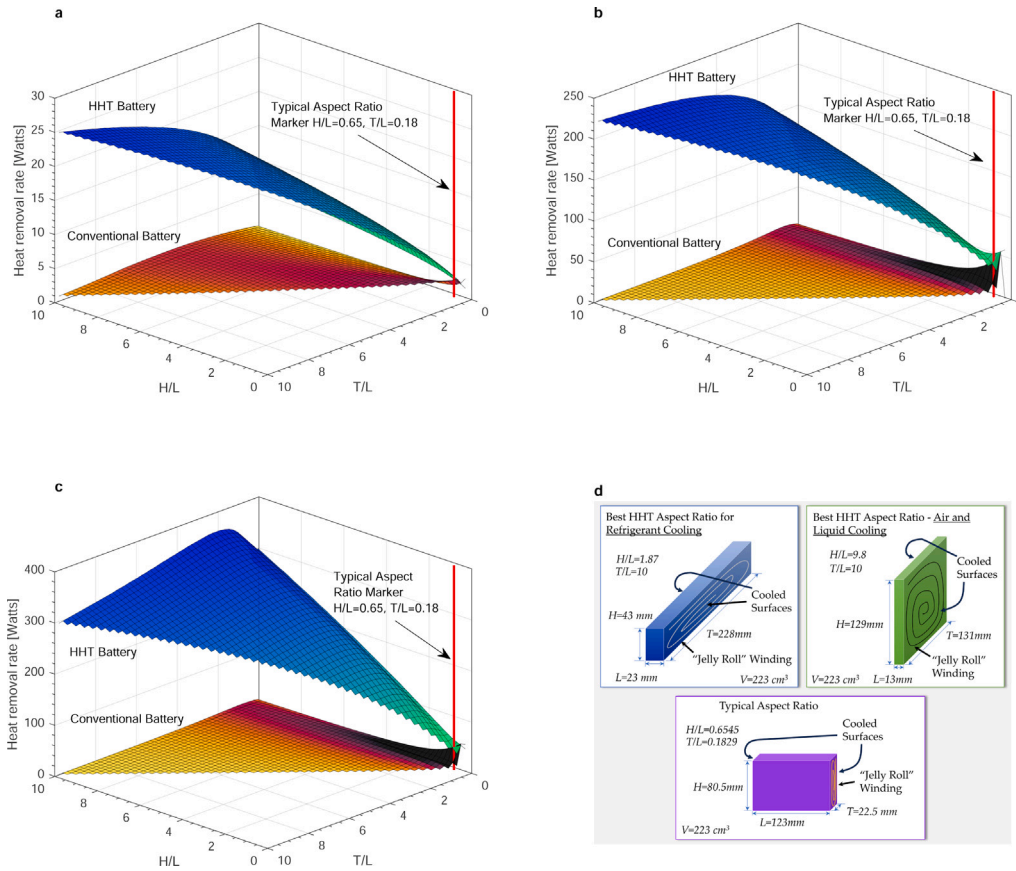


Fig. 10. (a) through (c), battery maximum heat generation vs. battery aspect ratio for both for HHT and conventional batteries. Heat generation maximum is defined as maximum heat generation that can be applied without exceeding the extreme conditions of 60 °C battery cell center temperature or 20 °C battery cell ΔT in x, y, or z-dimension with an ambient temperature 30 °C. (a) Air cooling, heat transfer coefficient 25 W/(m² K)⁻¹. (b) Liquid cooling, heat transfer coefficient 390 W/(m² K)⁻¹. (c) Refrigerant cooling, heat transfer coefficient 1740 W/(m² K)⁻¹. (d) Conceptualization of what selected aspect ratios from figure (a) through (c) would look like.

This asymptotic behavior indicates a point of diminishing returns with further increases in T/L. In contrast, the refrigerant-cooled case reaches a peak more steeply with increasing T/L before decreasing. The air and liquid cooling configurations may also experience a decline in performance if T/L is increased beyond what was modeled.

The heat removal rate as a function of H/L appears to increase almost linearly or at a constant rate for HHT across all cooling methods. This suggests that there could be additional performance gains with further increases in the H/L ratio. While manufacturing capabilities should be assessed, if manufacturers are currently limited to H/L ratios of 10, these results may serve as an incentive to innovate the battery manufacturing process, potentially opening up a new market for them. Additionally, it is important to note that the slope of the maximum heat removal rate with increasing H/L becomes steeper as the heat transfer coefficient increases for HHT batteries.

3.3. Explanation of the physics behind surface plot behavior

Each point on the response surfaces in Figs. 9c through d and 10a through c corresponds to the temperature or heat flow in a specific aspect ratio battery, modeled using the circuit diagram in Fig. 5b. Looking at Fig. 10a through c, as the T/L ratio increases, we observe a general trend across all cooling methods: the maximum heat removal rate increases, but the rate of increase slows down with further increases in T/L. For refrigerant cooling, the heat removal rate eventually starts to decrease after reaching its peak. These trends can be attributed to the net or equivalent thermal resistance of the model reaching a

minimum, at which point the heat removal rate peaks. As T/L increases while keeping H/L constant, the primary heat flow area in the R6 thermal path expands, reducing the thermal resistance of the HHT battery cell in the in-plane direction, as shown in Eq. (2). However, as T/L increases, the average distance that heat must travel from each battery current collector also increases, requiring a longer path to reach the center of the thermal connector. Once the heat reaches the center of the thermal connector, it must travel a longer distance to spread to its edges. Consequently, although the thermal resistance of the battery cell decreases with increasing T/L, the thermal resistance of the thermal connector increases. The net effect is an initial increase in the heat removal rate, driven by the lower thermal resistance of the battery cell. But as T/L continues to increase, the increasing thermal resistance of the thermal connector becomes more influential, leading to a reduction in the overall heat removal rate.

As H/L increases with constant T/L, we observe a nearly linear increase in the maximum heat removal rate. This is once again due to the combined effect of the dominant thermal resistances from both the battery and the thermal connectors. From Eq. (2), the area A of the R6 heat flow path increases directly with the height of the battery cell. Unlike T/L, the thermal resistance of the thermal connectors does not experience increasing heat flow distances as H/L increases, because the heat flow distance remains constant as H/L increases.

In summary, the response surfaces are shaped by the interplay of competing factors. The thermal resistance of the active portion of the battery cell decreases with increasing H/L and T/L, while the thermal resistance of the thermal connector increases with increasing T/L, but not with H/L. The net effect of these factors at any given point determines the overall shape of the response surfaces.

Table 5

Maximum heat removal rate for conventional and HHT batteries, both with typical aspect ratios using various cooling methods (air, liquid, and refrigerant).

Cooling method	Conventional battery [W]	HHT battery [W]	Cooling gain	Aspect ratio	
				H/L	T/L
Air	2.4	3.2	1.3×	0.65	0.18
Liquid	16.1	41.5	2.6×		
Refrigerant	17.5	45.7	2.6×		

Table 6

Comparison of maximum heat removal rate between a conventional battery with a typical aspect ratio and an HHT battery with an improved aspect ratio using various cooling methods (air, liquid, and refrigerant).

Cooling method	Conventional with typical aspect ratio [W]	HHT with improved aspect ratio [W]	Cooling gain	Aspect ratio	
				H/L	T/L
Air	2.4	24.8	10.3×	9.8	10
Liquid	16.1	220.7	13.7×	9.8	10
Refrigerant	17.5	362.3	20.7×	1.9	10

3.4. Summary and comparison of maximum heat removal rates and their corresponding aspect ratios

Table 5 summarizes a comparison of the maximum heat removal rate between a conventional battery and an HHT battery, both using the typical aspect ratio of the conventional target battery. At this aspect ratio, HHT batteries demonstrate a performance improvement ranging from 1.3X to 2.6X, depending on the cooling method and boundary conditions.

In contrast Table 5 which compares conventional and HHT batteries with typical aspect ratios, Table 6 compares a conventional battery with a typical aspect ratio to an HHT battery with an optimized aspect ratio. In this comparison, HHT batteries with improved aspect ratios show a maximum heat removal rate improvement of 10.3X to 20.7X over the conventional battery with the typical aspect ratio”.

3.5. Visualization of the ‘new’ HHT aspect ratios

Fig. 10d shows an example of the aspect ratios from Tables 5 and 6 which clearly differ from the typical aspect ratio of conventional batteries. However, these ‘new’ aspect ratios could present opportunities for battery thermal management designers, both for individual modules and entire packs, to explore creative ways to increase pack energy density and integrate novel cooling configurations. Additionally, they could open up potential intellectual property opportunities in the HHT battery thermal management space.

4. Discussion

4.1. Contextualizing HHT heat removal improvements and their impact on lithium-ion batteries and EVs

In the previous sections, it was demonstrated that HHT batteries have the potential for significant improvements in heat transfer capabilities compared to conventional batteries. However, these improvements require further context to understand their impact on overall battery performance. Below, we highlight several key areas of battery performance and explore how these enhanced heat transfer capabilities could influence them.

4.1.1. Extreme fast charging

Extreme fast charging of lithium-ion batteries faces several challenges, one of the main ones being the ability to dissipate heat at the rate it is generated during charging. The rate of Joule heat generation during charging can be calculated using the formula I^2R , where I is the current into the battery and R is the electrical resistance of the battery. For the target battery with a resistance of 2 mΩ [24], the heat generation at 15, 10, 5, and 3.5 min charging intervals is 20, 45,

180, and 363 W, respectively. When these heat generation values are compared with the heat removal rates in Tables 5 and 6 it becomes clear that, regardless of the cooling method used, conventional batteries cannot achieve a 15 min charge from a thermal standpoint. However, for the HHT battery with a typical aspect ratio, a 10 min charge could be feasible with either liquid or refrigerant cooling. For HHT battery with an improved aspect ratio, a 3.5 min charge could be achieved with refrigerant cooling, a 5 min charge with liquid cooling, and a 15 min charge with a simple, low-cost air cooling system.

4.1.2. Safety — thermal runaway mitigation

At the onset of thermal runaway, the battery generates more heat than it can dissipate, causing a rapid temperature rise. If the temperature reaches a critical threshold, an uncontrollable exothermic chain reaction may be triggered. From a thermal management perspective, the key factors in preventing thermal runaway are the system’s response rate and its maximum heat removal capacity. If the thermal management system can detect and respond quickly enough and has sufficient heat removal capacity in the onset stage, the battery could be prevented from reaching the critical temperature and thermal runaway can be avoided.

The thermal response of a battery or how fast it can respond to the cooling system can be measured by its time constant which is $\tau = RC$, where R is the thermal resistance of the battery and C is its thermal capacitance. The thermal resistance of the liquid cooled conventional, HHT with typical aspect ratio and HHT with improved aspect ratio are 1.9, 1.1 and 0.13 °C (W)⁻¹. The thermal capacitance is 624 J(°C)⁻¹. The time constants are 1186, 686 and 81 s respectively, indicating significantly smaller time constant and improved thermal response in the HHT batteries.

Battery self heating rates for thermal runaway start at zero and max out around 12–23 °C per minute [34–36]. With the equation $\dot{Q} = \rho V C_p \Delta T / t$, this equates to 124 to 240 W of heat generation.

These heat generation rates are within the capabilities of HHT batteries. Combined with the improved time constant (thermal response), there is potential for HHT batteries to thermally mitigate thermal runaway.

4.1.3. Extended battery life

Research has demonstrated that tab cooling with its in-plane cooling configuration, similar to HHT batteries, can increase battery lifespan by up to three times under high discharge rates, compared to surface-cooled batteries [22]. However, HHT batteries exhibit lower thermal resistance than the in-plane systems discussed in existing studies. According to the equation $\dot{Q}_{batt} = \Delta T_{batt} / R_{th\,batt}$, a significant reduction in $R_{th\,batt}$ allows the battery to operate at a lower ΔT_{batt} . High ΔT_{batt} is a key factor that reduces battery life. Additionally, operating at temperatures higher than the optimal range can further shorten battery

lifespan. A battery with a faster thermal response rate can remain closer to its optimal temperature for a longer period, which should, in turn, extend its overall lifespan. Therefore, HHT batteries, by utilizing in-plane cooling, lower ΔT_{batt} and a faster thermal response, have the potential to significantly improve battery life.

4.1.4. Reduced cold weather power loss

Cold temperatures reduce ion mobility in lithium-ion batteries, which limits the available power for vehicle acceleration. A potential solution to improve the customer experience is the rapid preheating of batteries prior to driving in cold weather, thus preventing power loss during use.

From a thermal management perspective, a battery with lower thermal resistance and a low time constant, such as an HHT battery, will respond to applied surface heating much more quickly than a conventional battery without these attributes. Therefore, it is expected that HHT batteries could significantly improve battery warm-up times, leading to better customer satisfaction in cold weather conditions.

4.1.5. Increased reliability

Battery reliability refers to the ability of a battery to consistently perform according to its key metrics over its lifespan. These metrics include capacity (Ah and Wh), state of charge (SOC), state of health (SOH), depth of discharge (DOD), cycle and calendar life, charge rate (C-Rate), energy density (Wh/kg, Wh/L), charge/discharge efficiency, coulombic efficiency, and open circuit voltage (OCV).

Effective battery thermal management is crucial for improving reliability. Key thermal management characteristics that enhance battery reliability include increasing heating and cooling rates to maintain the battery at an optimal temperature across varying environmental and operational conditions, reducing temperature gradients within the battery to ensure spatially uniform temperatures, and providing a faster thermal response to keep the battery closer to its optimal temperature for longer periods. HHT batteries significantly improve all of these thermal management characteristics, which could lead to a corresponding increase in battery reliability.

4.1.6. Lower costs

Due to their improved thermal management characteristics, HHT batteries could help reduce costs in several areas.

Lower battery costs - Studies have shown that using tab cooling to enable in-plane heat transfer like HHT batteries can reduce costs by 66% over surface cooling at high charge and high discharge rates [22]. These benefits came from uniform temperature of each battery layer. This is due to cooling being applied uniformly to each layer with the in-plane cooling configuration like HHT batteries.

Further studies have shown that to meet customer expectations for battery life, batteries are often over-sized to account for degradation and ensure a minimum level of performance at the end of their specified lifespan. However, research has also demonstrated that improving the battery thermal management system can reduce the need for oversizing. The cost savings from eliminating the need to oversize the battery can offset the investment in enhanced thermal management [5].

Battery thermal management system content reduction - HHT batteries have the potential to enhance heat transfer efficiency and decrease the power consumption of the battery thermal management system, while maintaining the same cooling rate.

Referring to Eq. (56), which represents the heat transfer from the battery,

$$\dot{Q}_{batt} = \frac{\Delta T_{batt}}{R_{th\ batt}} = \frac{(T_{batt\ center} - T_{batt\ surface})}{R_{th\ batt}} \quad (56)$$

It is shown that by lowering the battery's thermal resistance, a smaller ΔT_{batt} is required to maintain the same \dot{Q}_{batt} . If the battery center is kept at an optimal temperature, a reduced ΔT_{batt} means $T_{batt\ surface}$ will be increased. Now, considering Eq. (57), which represents the

upper limit for the Coefficient of Performance (COP), where COP is the efficiency of the cooling system. It becomes clear that increasing $T_{batt\ surface}$ can increase the COP/ efficiency of the system.

$$COP_{cooling} = \frac{T_C}{(T_H - T_C)} = \frac{(T_{batt\ surface})}{(T_{ambient} - T_{batt\ surface})} \quad (57)$$

The implications are that the thermal management system will draw less power from the batteries, resulting in an increased range. Moreover, a higher COP opens the possibility of downsizing the cooling system components, such as using a smaller compressor or fans that consume less power and reduce costs. Additionally, reducing the thickness of the condenser could decrease drag, further, reducing weight improving range and lowering costs. Similar efficiency improvements would be observed with both air and liquid cooling systems.

Reduced parts required for battery pack - In conventional batteries, the battery thickness may be limited to facilitate effective thermal management. However, with HHT batteries, the cells have the potential to be made thicker. Thicker cells could lead to a battery pack with fewer cells, reducing the number of components like bus bars, nuts, bolts, connectors, welds, and wires. As a result, material and labor costs could be lowered, and assembly time reduced. Additionally, the Battery Management System (BMS) could be made with less complexity.

4.1.7. Increased energy density

The rate of heat generation in batteries is known to increase with higher energy density [37]. To effectively implement batteries with greater energy density, enhanced thermal management systems will be crucial. With its exceptional heat transfer properties, HHT technology could facilitate the implementation of these higher energy density batteries.

5. Conclusion

Background and Context: Lithium-ion (Li-ion) batteries and associated thermal management technologies have made remarkable progress, driving the adoption of electric vehicles (EVs). However, to further accelerate the global energy transition and enhance EV adoption, continued advancements in Li-ion batteries are essential. Significant improvements in Battery Thermal Management (BTM) can play a critical role in this effort. Traditional BTM strategies primarily focus on improving heat transfer coefficients at the battery surface using air, liquid, or refrigerant cooling. While effective, these methods have drawbacks and may not be sustainable in the long term. In contrast, less attention has been paid to reducing the battery's thermal resistance, which is a significant bottleneck to efficient heat dissipation.

Proposed Solution: This work introduces a novel approach: a reduced thermal resistance, high-heat transfer (HHT) battery technology. Unlike previous designs, the HHT battery is specifically engineered to optimize thermal performance. It features in-plane heat transfer, optimized geometry, low thermal resistances, minimal thermal interface resistances, and thermal bridging to achieve superior heat dissipation.

Validation and Performance: A battery thermal model based on equivalent electrical-thermal circuit analogies is developed for speed and accuracy. The model is validated against experimental data from the literature, showing strong correlation and ensuring reliable real-world performance predictions. Thermal performance metrics for both conventional and HHT batteries are compared in a parametric study using air, liquid, and refrigerant boundary conditions across a range of aspect ratios. HHT batteries demonstrate heat removal rates up to 20 times higher than conventional batteries, marking a major breakthrough in overcoming thermal challenges that limit Li-ion battery performance.

Implications and Potential: The potential implications of this technology are significant. From a heat dissipation standpoint, the HHT battery with a typical aspect ratio can achieve a 10 min charge

using either liquid or refrigerant cooling. With an improved aspect ratio, the HHT battery could achieve a 3.5 min charge with refrigerant cooling, a 5 min charge with liquid cooling, and a 15 min charge with a simple, low-cost air-cooling system. The thermal response times, measured by their time constant, for conventional batteries, typical aspect ratio HHT batteries, and enhanced aspect ratio HHT batteries are 1186, 686, and 81 s, respectively. With their fast thermal response and high heat transfer rates, HHT batteries have the potential to thermally mitigate battery thermal runaway. Due to high heat transfer rates, uniform temperatures, and fast thermal response, opportunities are also explored in areas such as battery life, reduced cold-weather power loss through rapid battery preheating, increased reliability, lower battery pack costs, reduced BTMS power consumption, and higher energy density. These advancements could dramatically improve the affordability and performance of electric vehicles, accelerating their widespread adoption.

Future Work: While the study explored a range of aspect ratios, the non-typical ones have not yet been confirmed as manufacturable. However, the significant potential of HHT batteries suggests that, even if these aspect ratios are not currently manufacturable, the technology could drive innovation in battery manufacturing. Additionally, the typical aspect ratios, which are known to be manufacturable, already demonstrate substantial improvements over conventional batteries.

Conclusion: In conclusion, HHT battery technology represents a transformative advancement in addressing the thermal management challenges of Li-ion batteries. By enabling faster charging, enhancing safety, extending battery life, and reducing costs, HHT technology has the potential to significantly improve the performance and affordability of electric vehicles. While further real-world testing and full range manufacturability studies are needed, this innovation paves the way for future breakthroughs in battery design, supporting the global energy transformation and accelerating the adoption of electric vehicles.

Declaration of competing interest

The authors declare the following financial interests/personal relationships which may be considered as potential competing interests: Alfred Piggott has patent issued to Applied Thermoelectric Solutions LLC. If there are other authors, they declare that they have no known competing financial interests or personal relationships that could have appeared to influence the work reported in this paper.

Acknowledgment

This research did not receive any specific grant from funding agencies in the public, commercial, or not-for-profit sectors.

Data availability

Everything needed to recreate the model is included in the paper.

References

- [1] T.W. House, FACT SHEET: President Biden announces steps to drive American leadership forward on clean cars and trucks, 2021, [Online]. Available: <https://www.whitehouse.gov/briefing-room/statements-releases/2021/08/05/fact-sheet-president-biden-announces-steps-to-drive-american-leadership-forward-on-clean-cars-and-trucks/>.
- [2] ARPA-E, Electric vehicles for American low-carbon living, 2022, [Online]. Available: <http://arpa-e.energy.gov/technologies/programs/evs4all>.
- [3] S. Liu, G. Zhang, C.-Y. Wang, Challenges and innovations of lithium-ion battery thermal management under extreme conditions: A review, *ASME J. Heat Mass Transf.* 145 (8) (2023) 080801, [Online]. Available: <https://asmedigitalcollection.asme.org/heattransfer/article/145/8/080801/1156583/Challenges-and-Innovations-of-Lithium-Ion-Battery>.
- [4] Y. Ortiz, P. Arévalo, D. Peña, F. Jurado, Recent advances in thermal management strategies for lithium-ion batteries: A comprehensive review, *Batteries* 10 (3) (2024) 83, [Online]. Available: <https://www.mdpi.com/2313-0105/10/3/83>.
- [5] J.P. Rugh, A. Pesaran, K. Smith, Electric Vehicle Battery Thermal Issues and Thermal Management Techniques, NREL/PR-5400-52818, Scottsdale Arizona, 2011, [Online]. Available: <https://www.nrel.gov/docs/fy13osti/52818.pdf>.
- [6] M. Keyser, Thermal Implications for Extreme Fast Charge, Vehicle Technologies Office (VTO) Annual Merit Review and Peer Reptot Number: NREL/PR-5400-68339, National Renewable Energy Laboratory, Washington, D.C., 2017, [Online]. Available: <https://www.nrel.gov/docs/fy17osti/68339.pdf>.
- [7] K. Smith, E. Wood, J. Neubauer, J. Myungsoo, P. Ahmad, Models for battery reliability and lifetime, in: Battery Congress 2013, Ann Arbor, Michigan, 2013, [Online]. Available: <https://www.nrel.gov/docs/fy14osti/57746.pdf>.
- [8] J. Hou, L. Lu, L. Wang, A. Ohma, D. Ren, X. Feng, Y. Li, Y. Li, I. Ootani, X. Han, W. Ren, X. He, Y. Nitta, M. Ouyang, Thermal runaway of Lithium-ion batteries employing LiN(SO₂F)₂-based concentrated electrolytes, *Nat. Commun.* 11 (1) (2020) 5100.
- [9] W. Li, Y. Xue, X. Feng, J. Liu, F. Zhang, S. Rao, T. Zhang, Z. Gao, Z. Du, C. Ni, J. Shi, H. Wang, C. Rong, D. Wang, Enhancing understanding of particle emissions from lithium-ion traction batteries during thermal runaway: An overview and challenges, *ETransportation* 22 (2024) 100354, [Online]. Available: <https://www.sciencedirect.com/science/article/pii/S2590116824000444>.
- [10] H. Wang, Y. Zhang, W. Li, Z. Gao, B. Zhang, M. Ouyang, Experimental study on the cell-jet temperatures of abused prismatic Ni-rich automotive batteries under medium and high states of charge, *Appl. Therm. Eng.* 202 (2022) 117859, [Online]. Available: <https://www.sciencedirect.com/science/article/pii/S1359431121012837>.
- [11] A. Kumar Thakur, R. Sathyamurthy, R. Velraj, R. Saidur, A.K. Pandey, Z. Ma, P. Singh, S.K. Hazra, S. Wafa Sharshir, R. Prabakaran, S.C. Kim, S. Panchal, H.M. Ali, A state-of-the art review on advancing battery thermal management systems for fast-charging, *Appl. Therm. Eng.* 226 (2023) 120303, [Online]. Available: <https://www.sciencedirect.com/science/article/pii/S1359431123003320>.
- [12] H. Lundgren, P. Svens, H. Ekström, C. Tengstedt, J. Lindström, M. Behm, G. Lindbergh, Thermal management of large-format prismatic lithium-ion battery in PHEV application, *J. Electrochem. Soc.* 163 (2) (2015) A309, [Online]. Available: <https://iopscience.iop.org/article/10.1149/2.09411602jes/meta>.
- [13] B. Wu, Y. Yang, D. Liu, C. Niu, M. Gross, L. Seymour, H. Lee, P.M.L. Le, T.D. Vo, Z.D. Deng, E.J. Dufek, M.S. Whittingham, J. Liu, J. Xiao, Good practices for rechargeable lithium metal batteries, *J. Electrochem. Soc.* 166 (16) (2019) A4141, [Online]. Available: <https://iopscience.iop.org/article/10.1149/2.0691916jes/meta>.
- [14] R. Christen, G. Rizzo, A. Gadola, M. Stöck, Test method for thermal characterization of li-ion cells and verification of cooling concepts, *Batteries* 3 (1) (2017) 3, [Online]. Available: <https://www.mdpi.com/2313-0105/3/1/3>.
- [15] O. Kalkan, A. Celen, K. Bakirci, Experimental and numerical investigation of the LiFePO₄ battery cooling by natural convection, *J. Energy Storage* 40 (2021) 102796, [Online]. Available: <https://www.sciencedirect.com/science/article/pii/S2352152X21005235>.
- [16] T. Wang, K.J. Tseng, J. Zhao, Z. Wei, Thermal investigation of lithium-ion battery module with different cell arrangement structures and forced air-cooling strategies, *Appl. Energy* 134 (2014) 229–238, [Online]. Available: <https://www.sciencedirect.com/science/article/pii/S0306261914008162>.
- [17] J. Kim, J. Oh, H. Lee, Review on battery thermal management system for electric vehicles, *Appl. Therm. Eng.* 149 (2019) 192–212, [Online]. Available: <https://www.sciencedirect.com/science/article/pii/S135943111835614X>.
- [18] M. Suresh Patil, J.-H. Seo, M.-Y. Lee, A novel dielectric fluid immersion cooling technology for Li-ion battery thermal management, *Energy Convers. Manage.* 229 (2021) 113715, [Online]. Available: <https://linkinghub.elsevier.com/retrieve/pii/S0196890420312395>.
- [19] Y. Zhu, Y. Fang, L. Su, Y. Fei, Experimental study on thermal performance of a pumped two-phase battery thermal management system, *Int. J. Energy Res.* 44 (6) (2020) 4664–4676, [Online]. Available: <https://onlinelibrary.wiley.com/doi/abs/10.1002/er.5247>.
- [20] United states advanced battery consortium (USABC), [Online]. Available: <https://uscar.org/download/246/energy-storage-system-goals/12843/thermal-management-system-goals.pdf>.
- [21] S. Li, C. Zhang, Y. Zhao, G.J. Offer, M. Marinescu, Effect of thermal gradients on inhomogeneous degradation in lithium-ion batteries, *Commun. Eng.* 2 (1) (2023) 1–14, [Online]. Available: <https://www.nature.com/articles/s44172-023-00124-w>.
- [22] I.A. Hunt, Y. Zhao, Y. Patel, G.J. Offer, Surface cooling causes accelerated degradation compared to tab cooling for lithium-ion pouch cells, *J. Electrochem. Soc.* 163 (9) (2016) A1846, [Online]. Available: <https://iopscience.iop.org/article/10.1149/2.0361609jes/meta>.
- [23] A. Piggott, ParaThermic® battery thermal management, 2024, [Online]. Available: <https://thermoelectricsolutions.com/parathermic-battery-thermal-management/>.
- [24] J. Kleiner, L. Komsyska, G. Elger, C. Endisch, Thermal modelling of a prismatic lithium-ion cell in a battery electric vehicle environment: Influences of the experimental validation setup, *Energies* 13 (1) (2020) 62, [Online]. Available: <https://www.mdpi.com/1996-1073/13/1/62>.

- [25] A. Robertson, D. Gross, An electrical-analog method for transient heat-flow analysis, *J. Res. Natl. Bur. Stand.* 61 (2) (1958) 105, [Online]. Available: https://nvlpubs.nist.gov/nistpubs/jres/61/jresv61n2p105_A1b.pdf.
- [26] E. Cheever, SCAM - A tool for symbolic solution of circuit equations. [Online]. Available: <https://cheever.domains.swarthmore.edu/Ref/mna/MNA6.html>.
- [27] S. Narumanchi, M. Mihalic, K. Kelly, G. Eesley, Thermal interface materials for power electronics applications, in: 2008 11th Intersociety Conference on Thermal and Thermomechanical Phenomena in Electronic Systems, IEEE, Orlando, FL, USA, 2008, pp. 395–404, [Online]. Available: <http://ieeexplore.ieee.org/document/4544297/>.
- [28] L.W. Zhang, Y.S. Yu, Simulation of thermal characteristics of lithium batteries for electric vehicles, *IOP Conf. Ser.: Mater. Sci. Eng.* 657 (1) (2019) 012036, [Online]. Available: <https://iopscience.iop.org/article/10.1088/1757-899X/657/1/012036>.
- [29] S.J. Eckels, T.M. Doerr, M.B. Pate, Heat transfer coefficients and pressure drops for R-134a and an ester lubricant mixture in a smooth tube and a micro-fine tube, *ASHRAE Trans.* 104 (1a) (1998) 366–375, [Online]. Available: <https://www.osti.gov/biblio/653206>.
- [30] Y. Wang, Q. Gao, H. Wang, Structural design and its thermal management performance for battery modules based on refrigerant cooling method, *Int. J. Energy Res.* 45 (3) (2021) 3821–3837, [Online]. Available: <https://onlinelibrary.wiley.com/doi/abs/10.1002/er.6035>, eprint: <https://onlinelibrary.wiley.com/doi/pdf/10.1002/er.6035>.
- [31] D. Jung, D.N. Assanis, Numerical Modeling of Cross Flow Compact Heat Exchanger with Louvered Fins using Thermal Resistance Concept, SAE Technical Paper 2006-01-0726, SAE International, Warrendale, PA, 2006, [Online]. Available: <https://www.sae.org/publications/technical-papers/content/2006-01-0726/>, Citation Key:.
- [32] I.M.A. Aljubury, M.A. Mohammed, Heat transfer analysis of conventional round tube and microchannel condensers in automotive air conditioning system, *J. Eng.* 25 (2) (2019) 38–56, [Online]. Available: <https://joe.uobaghdad.edu.iq/index.php/main/article/view/735>.
- [33] REOTEMP, Thermocouple accuracies - Thermocouple accuracy - Thermocouple accuracy comparison chart. [Online]. Available: <https://www.thermocoupleinfo.com/thermocouple-accuracies.htm>.
- [34] D.H. Doughty, E.P. Roth, A general discussion of li ion battery safety, *Electrochem. Soc. Interface* 21 (2) (2012) 37, [Online]. Available: <https://iopscience.iop.org/article/10.1149/2.F03122if/meta>.
- [35] M. Karp, Thermal Runaway Initiation Methods for Lithium Batteries, Tech. Rep. DOT/FAA/TC-20/12, U.S. Department of Transportation Federal Aviation Administration, William J. Hughes Technical Center Aviation Research Division Atlantic City International Airport New Jersey 08405, 2019, [Online]. Available: <https://www.fire.tc.faa.gov/pdf/tc20-12.pdf>.
- [36] D.H. Doughty, Vehicle Battery Safety Roadmap Guidance, Tech. Rep. NREL/SR-5400-54404, 1055366, National Renewable Energy Laboratory, 2012, [Online]. Available: <http://www.osti.gov/servlets/purl/1055366/>.
- [37] A. Saxon, C. Yang, S. Santhanagopalan, M. Keyser, A. Colclasure, Li-ion battery thermal characterization for thermal management design, *Batteries* 10 (4) (2024) 136, [Online]. Available: <https://www.mdpi.com/2313-0105/10/4/136>.